SAGE III Algorithm Theoretical Basis Document (ATBD)
Solar and Lunar Algorithm

Compiled by the SAGE III ATBD Team

LaRC 475-00-109
Version 2.1
26 March 2002

TABLE OF CONTENTS

CHANGE RECORD PAGE

ISSUE	DATE	PAGES AFFECTED	DESCRIPTION
Baseline	November 10, 2000	All	Supersedes: 1) SAGE III Water Vapor Algorithm Theoretical Basis Document, LaRC 475-00-100, Release 1.2, dated February 18, 2000. 2) SAGE III Nitrogen Dioxide Algorithm Theoretical Basis Document, LaRC 475-00-101, Release 1.2, dated February 18, 2000. 3) SAGE III Nitrogen Trioxide Algorithm Theoretical Basis Document, LaRC 475-00-102, Release 1.2, dated February 18, 2000. 4) SAGE III Chlorine Dioxide Algorithm Theoretical Basis Document, LaRC 475-00-103, Release 1.2, dated February 18, 2000. 5) SAGE III Temperature & Pressure Algorithm Theoretical Basis Document, LaRC 475-00-104, Release 1.2, dated February 18, 2000. 6) SAGE III Aerosol Algorithm Theoretical Basis Document, LaRC 475-00-105, Release 1.2, dated February 18, 2000. 7) SAGE III Ozone Algorithm Theoretical Basis Document, LaRC 475-00-107, Release 1.2, dated February 18, 2000. as referenced in the ESDIS/SAGE III IPA; GSFC 423-010-37 and ESSPO/SAGE III API SOW; LaRC475-00-01.
Version 2.1	March 26, 2002	Section 1.5; p. 3 Table 1.6.1; p.5	Added contributing authors Removed references to mixing ratio profiles

1.0 Introduction

The Stratospheric Aerosol and Gas Experiment III (SAGE III) is a critical part of the Earth Observing System (EOS). The EOS mission is to develop an understanding of the total Earth system and the effects of natural and human-induced changes on the global environment. SAGE III provides limb occultation measurements with a flexible instrument design that permits on orbit reprogramming and channel selection with up to 809 channels spanning the ultraviolet, visible, and near infrared (280-1040 nm). Solar observations will provide high resolution vertical profiles of multi-wavelength aerosol extinction, the molecular density of ozone, nitrogen dioxide, and water vapor, as well as profiles of temperature, pressure, and cloud presence. In addition, the inclusion of a repositionable solar attenuator will allow lunar occultation observations that will improve the geographic coverage and permit measurements of nitrogen trioxide and chlorine dioxide in addition to ozone, nitrogen dioxide, water vapor, and pressure.

1.1 Purpose

This Algorithm Theoretical Basis Document (ATBD) describes the algorithms used to retrieve the SAGE III Solar and Lunar species data products. All SAGE III data products will be archived at the NASA Langley Research Center's Atmospheric Science Data Center (ASDC) (formerly the Langley Research Center Distributed Active Archive Center). This document identifies sources of input data, which are required for the retrieval, provides the physical theory and mathematical background underlying the use of this information in the retrievals, describes practical considerations affecting algorithm development, and outlines a test and validation approach. Chapter 2 provides background information on the instrument technique and relevance to the EOS mission. Chapter 3 provides a discussion the solar retrieval algorithm. This chapter also includes details on the form and quality of the transmission measurements (level 1B data products) A discussion of the lunar retrieval algorithm is provided in Chapter 4. Additional information on instrument design, retrieval algorithm is approximations, spectroscopic database is provided in Appendices A-D.

1.2 Scope

This document covers the algorithm theoretical basis for the parameters to be included in the SAGE III Data Products at or near launch time. Only parameters that are to be routinely retrieved are discussed. Current development and prototyping efforts may result in modifications to parts of certain algorithms. Only the algorithms which are implemented for routine processing of SAGE III data will be preserved in the release of this document.

1.3 Applicable Documents

1.3.1 Controlling Documents

EOS Science Plan, NASA HQ EOS, January 1999.

Mission to Planet Earth Strategic Enterprise Plan 1996-2002, NASA HQ EOS, May 1996.

Execution Phase Project Plan for Earth Observing System (EOS), GSFC 170-01-01, Rev. A., May 1995.

1.3.2 SAGE III ATDB Reference Documents

SAGE III Algorithm Theoretical Basis Document: Transmission Data Products, LaRC 475-00-108, November 2000.

SAGE III Algorithm Theoretical Basis Document: Cloud Presence Data Products, LaRC 475-00-106, November 2000.

SAGE III Algorithm Theoretical Basis Document (ATBD) Solar and Lunar Algorithm, LaRC 475-00-109, November 2000.

1.4 Revision History

The original version of this document was dated November 15, 1996. Version 1.1 was released on 15 April 1997. Version 1.2 was released on 18 February 2000. Version 2.0 was released on 10 November 2000. This release, version 2.1, is dated March 2002.

1.5 Contributing Authors

The SAGE III ATBDs were drafted by a team of SAGE III science team members and SAGE III science cadre, led by one of the science team members. The entire team participated in oral and written revisions of the methodology and documentation as part of the SAGE III science team meetings and research activities.

Contributing Authors	**Affiliation**
Colette Brogniez	University de Lille, France
Er-Woon Chiou	SAIC
William P. Chu	NASA Langley Research Center
Albert A. Chernikov	Central Aerological Observatory
Derek M. Cunnold	Georgia Tech
John DeLuisi	NOAA
Philip A. Durkee	Naval Postgraduate School
Nikolai F. Elansky	Russian Academy of Science
Benjamin M. Herman	University of Arizona
Peter V. Hobbs	University of Washington
Geoff S. Kent	Science and Technology Corporation
Jacqueline Lenoble	University de Lille, France
M. P. McCormick, Principal Investigator	Hampton University
Hope A. Michelsen	AER
Alvin J. Miller	NOAA/NCEPS
Volker Mohnen	State University of New York at Albany
Randy Moore	SAIC
Michael C. Pitts	NASA Langley Research Center
Lamont R. Poole	NASA Langley Research Center
Venkatachalam Ramaswamy	Princeton University
David Rind	Goddard Institute for Space Studies
David Risley	SAIC
Michael W. Rowland	SAIC
Philip B. Russell	NASA Ames Research Center
Vinod K. Saxena	North Carolina State University
Eric P. Shettle	Naval Research Laboratory
Victor E. Sothcott	SAIC
Ghassan Taha	University of Arizona
Larry W. Thomason	NASA Langley Research Center
Charles R. Trepte	NASA Langley Research Center
Gabor Vali	University of Wyoming
Lelia B. Vann	NASA Langley Research Center
Robert E. Veiga	SAIC
Pi-Huan Wang	Science and Technology Corporation
Steven C. Wofsy	Harvard University

David C. Woods	NASA Langley Research Center
Joseph M. Zawodny	NASA Langley Research Center

Technical assistance was provided by Jackie Bumgardner, Kathy Drummond and Susan Walters.

1.6 SAGE III Standard Data Products

Table 1.6.1 SAGE III standard data products

PRODUCT NAME	**UNCERTAINTY Systematic :: Precision**	**TEMPORAL RESOLUTION**	**HORIZONTAL Resolution :: Coverage**	**VERTICAL Resolution :: Coverage**
Level 1B Transmission (≤80 wavelengths) Solar Events	0.05% :: 0.05%	1/(2 minutes), 30/day	<2 x <1 deg :: Global	0.5 km :: 0-100 km
Aerosol Extinction Stratospheric Optical Depth (at 9 wavelength bands), Aerosol to molecular/extinction ratio at 1020 nm (solar only)	5% :: 5%	1/(2 minutes), 30/day	<2 x <1 deg :: Global	0.5 km :: 0-40 km
O_3 Concentration Slant Path Col. Density	6% :: 5%	1/(2 minutes), 30/day	<2 x <1 deg :: Global	0.5 km :: 6-85 km 0.5 km :: 50-85 km
NO_2 Concentration Slant Path Col. Density	10% :: 15%	1/(2 minutes), 30/day	<2 x <1 deg :: Global	0.5 km :: 10-50 km 0.5 km :: 10-50 km
H_2O Concentration	10% :: 15%	1/(2 minutes), 30/day	<2 x <1 deg :: Global	0.5 km :: 0-50 km
NO_3 (Lunar Only) Concentration	10% :: 10%	1/(2 minutes), ≤30/day	<2 x <1 deg :: Global	0.5 km :: 20-55 km
OClO (Lunar Only) Concentration	25% :: 20%	1/(2 minutes), ≤30/day	<2 x <1 deg :: Global	0.5 km :: 15-25 km
Pressure	2% :: 2%	1/(2 minutes), 30/day	<2 x <1 deg :: Global	0.5 km :: 0-85 km 1000-0.004 hPa
Temperature Profile	2K :: 2K	1/(2 minutes), 30/day	<2 x <1 deg :: Global	0.5 km :: 0-85 km
Cloud Presence	N/A	1/(2 minutes), 30/day	<2 x <1 deg :: Global	0.5 km :: 6-30 km

2.0 Background

SAGE III is the fifth generation of solar occultation instruments designed to measure atmospheric aerosols and gaseous species in the atmosphere. The solar occultation method employs the attenuation of the Sun's rays as observed through the limb of the Earth's atmosphere to determine the vertical distribution of important atmospheric constituents. Measurements are made during each sunrise and sunset (an "event") encountered by the spacecraft (~30/day). This method is well suited for long-term monitoring of trends and variability in key species such as ozone since the instrument is recalibrated during each event. The instrument concept originated as a hand-held, single wavelength sunphotometer (Stratospheric Aerosol Measurement or SAM) which was flown onboard an Apollo mission in 1975 [Pepin and McCormick, 1976]. SAM II was a one wavelength (1000 nm) instrument which operated on Nimbus-7 between 1978 and 1994 [McCormick *et al.,* 1979, 1981]. The Stratospheric Aerosol and Gas Experiment (SAGE) operated on the Application Explorer Mission 2 (AEM-2) spacecraft between 1979 and 1981. This instrument made measurements at 4 wavelengths and measured molecular density profiles of O_3 and NO_2 in addition to aerosol extinction at 2 wavelengths (450 and 1000 nm) [McCormick *et al*., 1979]. SAGE II has operated on the Earth Radiation Budget Satellite (ERBS) since 1984 and makes measurements at 7 wavelengths. In addition to the species measured by SAGE, SAGE II measures the molecular density profile of H_2O and aerosol extinction at 4 wavelengths (385, 453, 525 and 1020 nm) [Mauldin, 1985; McCormick, 1987]. In SAGE III, a charged coupled device (CCD) linear array provides spectral coverage from 280 to 1040 nm. In addition, a single photodiode adds aerosol extinction measurements at 1550 nm. [McCormick *et al*., 1991; Mauldin *et al*., 1989; McCormick *et al*., 1993]. A repositionable solar attenuator will permit both solar and lunar occultation measurements, increasing the geographical coverage and allowing for the detection of nitrogen trioxide and chlorine dioxide. The incorporation of the CCD array will permit the measurement of gaseous species from multichannel absorption signatures simplifying the retrieval process, and 16-bit digitization will improve the precision and altitude range of the measurements.

2.1 Experimental Objectives

The science objectives to be accomplished by SAGE III are:

- Retrieve global profiles of atmospheric aerosol extinction, temperature, and pressure and molecular density profiles of ozone, water vapor, nitrogen dioxide, nitrogen trioxide, and chlorine dioxide with 0.5 km vertical resolution.

- Characterize tropospheric as well as stratospheric clouds and investigate their effects on the Earth's environment, including radiative, microphysical, and chemical interactions.

• Determine long-term trends in gaseous species and temperature.

• Provide atmospheric data essential for the interpretation and calibration of other satellite sensors, including EOS instruments.

• Investigate the spatial and temporal variability of these species in order to determine their role in climate processes, biogeochemical cycles, and the hydrological cycle.

2.2 Relevance of Measurements to EOS

2.2.1 Ozone

Ozone research has remained at the forefront of atmospheric science for many years because stratospheric ozone shields the Earth's surface (and its inhabitants) from harmful ultraviolet radiation. Since recent declines in stratospheric ozone have been linked to human activity, accurate long-term measurements of ozone remain crucial. SAGE III ozone measurements will provide important contributions in the following areas:

• Large and poorly understood long-term changes have been observed in the lower stratosphere and upper troposphere. SAGE III's high vertical resolution and long-term stability make it uniquely well suited to make these measurements.

• The relationship between aerosol, cloud, and chemical processes affecting ozone requires simultaneous measurements of these atmospheric constituents (such as those made by SAGE III).

• Ozone is a strong greenhouse gas that modifies the macroscopic structure of the atmosphere. Changes in the amount of stratospheric ozone can lead to changes in sensible weather at the Earth's surface. Accurate simulations of climate change require accurate assessments of changes in ozone levels.

• Changing levels of ozone can also cause changes in other chemically and radiatively important gases including methane and the hydroxyl radical.

• Ozone can also be used as a tracer of dynamic processes in the lower stratosphere which are difficult to directly observe. These include the transport of air from the tropics to mid-latitudes.

2.2.2 Water Vapor

On a molecule-by-molecule basis, water vapor is the predominant greenhouse gas and plays a crucial role in regulating the global climate system. An improved understanding of the global water vapor distribution can enhance our ability to understand water's role

in climate processes. SAGE III water vapor measurements will provide important contributions in the following areas:

• Reduced uncertainties in the upper tropospheric moisture field used for weather forecast model initialization, especially in the tropics.

• The long-term stability and self-calibration capabilities of SAGE III may permit the detection of a trend in water vapor in the upper troposphere and lower stratosphere as a diagnostic of global warming.

• SAGE III water vapor observations will provide valuable information to help EOS observation facilities evaluate, and correct for, water vapor induced variations in remotely measured parameters.

• High vertical resolution water vapor profiles will help illuminate hydrological processes in the atmosphere such as the tropical "tape-recorder."

2.2.3 Aerosols

Aerosols play an essential role in the radiative and chemical processes that govern the Earth's climate. Since stratospheric aerosol loading has varied by a factor of 30 since 1979, long-term monitoring of tropospheric and stratospheric aerosol is crucial. SAGE III aerosol measurements will provide important contributions in the following areas:

• Research demonstrates that the long-term variability of aerosol abundance strongly modulates the rate of ozone destruction in the lower stratosphere [Solomon *et al.,* 1997].

• The impact of aircraft exhaust on ozone is strongly dependent on the abundance and properties of the ambient aerosol. The future of high speed, stratospheric air travel is, in part, dependent on improved understanding of aerosol properties [Stolarski and Weosky, 1993].

• Aerosol radiative forcing is the largest unknown in current climate models and, as a result, in predicting future climate. Accurate vertically-resolved measurements of aerosol optical properties are an important element of improved climate prediction [IPCC, 1996].

• Observations from space of many geophysical properties like sea surface temperature, vegetation, and atmospheric trace gas species can be adversely affected by the presence of aerosol. Other EOS sensors like MODIS and MISR require SAGE III measurements of stratospheric aerosols to achieve optimal performance.

2.2.4 Nitrogen Dioxide, Nitrogen Trixoide, and Chlorine Dioxide

Nitrogen dioxide (NO_2), nitrogen trixoide (NO_3), and chlorine dioxide (OClO) play crucial roles in stratospheric chemistry and the catalytic cycles that destroy stratospheric ozone. SAGE III measurements will provide important contributions in the following areas:

- SAGE III NO_2 measurements are important because the processes that occur in the polar vortex during winter and spring and give rise to the ozone hole effectively convert NO_2 to nitric acid (HNO_3). Monitoring NO_2 abundance, thus provides an important diagnostic of ozone hole chemistry.

- Since it is measured during both solar and lunar occultation events, SAGE III observations of NO_2 will improve our understanding of the strong diurnal (daily) cycles in stratospheric processes.

- SAGE III will make virtually unique measurements of nitrogen trixoide (NO_3). Although it is short lived in the presence of sunlight, NO_3 plays an active role in the chemistry of other reactive nitrogen species such as NO_2 and dinitrogen pentoxide (N_2O_5) and, thus, indirectly in ozone chemistry.

- Since few other measurements of NO_3 are available, SAGE III measurements, which are made during lunar occultation (nighttime) events, will provide crucial validation for our current understanding of reactive nitrogen chemistry.

- The unique SAGE III observations of chlorine dioxide (OClO) will provide insight into nocturnal polar chemical processes that set the stage for the ozone loss observed at high latitudes in the spring.

2.2.5 Pressure and Temperature

SAGE III temperature measurements will provide a unique data set for monitoring and understanding atmospheric temperature changes. In particular, the long-term stability and self-calibration capabilities of SAGE III may permit the detection of trends in stratospheric and mesospheric temperature that would be important diagnostics of climate change. SAGE III temperature measurements will provide important contributions in the following areas:

- SAGE III temperature measurements in the upper stratosphere and mesosphere will be the only source of long-term temperature measurements in this region of the atmosphere.

- Short-term temperature variations are important in understanding the photochemical interactions and feedback in the formation and destruction of stratospheric ozone.

• SAGE III temperature measurements will allow the monitoring of periodic temperature changes, such as those associated with the solar cycle and quasi-biennial oscillation, and the effects of radiative forcing by aerosols.

• An improved temperature climatology will lead to better radiative-dynamical-chemical general circulation models and enhance the understanding of the interactions between these processes and the state of the climate system.

• Temperature and pressure measurements are essential to SAGE III for computing molecular scattering and the retrieval of mass mixing ratios of gaseous species on pressure surfaces.

3.0 Solar Algorithm Description

3.1 Introduction

3.1.1 Physical Description

SAGE III is designed to measure the attenuation of solar radiation by the Earth's atmosphere due to scattering and absorption by atmospheric constituents during each sunrise and sunset encountered by its spaceborne platform. In addition, SAGE III will make measurements during moonrise and moonset when the atmosphere is not directly illuminated by the Sun. SAGE III consists of three subsystems: the pointing, the imaging, and the spectrometer subsystems. The pointing subsystem consists of a scan mirror which acquires the radiant target (either the Sun or the Moon), and performs vertical scanning (with respect to the Earth's horizon) across the target. A measurement is considered to occur at the point along the line of sight (LOS) from the instrument to the target at which it comes closest to the Earth's surface (i.e., the sub-tangent point). The altitude of that point above the Earth's surface is commonly referred to as the tangent altitude. The imaging subsystem produces a focused image of the target at a focal plane where the "science" aperture, that defines the instrument's instantaneous field of view (IFOV), is situated. The SAGE III IFOV is 30 arcseconds in the vertical direction which translates to approximately 0.5 km at the tangent altitude. The spectrometer subsystem is situated behind the science aperture and consists of an 809-element CCD to measure solar radiation from 280 to 1040 nm with 1 to 2 nm spectral resolution. An additional photodetector is used to measure radiation at 1550 nm.

The viewing geometry of a solar occultation event is illustrated in Figure 3.1.1. During an event, the spacecraft motion relative to the Sun's (or Moon's) location permit the measurement of atmospheric transmission at tangent altitudes from the Earth's surface to well above the atmosphere. Since the instrument continually scans vertically across the target, and both the Sun and Moon subtend 32 arcminutes, the transmission at each tangent altitude is measured many times during an event. In addition, by measuring the unattenuated target (along LOS's which do not intersect the Earth's atmosphere) the instrument is recalibrated during each event. Therefore, the instrument provides not only accurate, high vertical resolution measurements of atmospheric transmission, but measurements which are relatively immune to drift in instrument performance.

Figure 3.1.2 illustrates the operation of the SAGE III instrument during a typical sunrise event. The two solid lines in the figure represent the upper and lower edges of the Sun as viewed from the spacecraft during the course of the event. The apparent narrowing of the solar image in the lower atmosphere is the result of refraction. The "saw-tooth" line represents the relative motion of the instrument mirror as it scans across the Sun at a nominal rate of 15 arcminutes s^{-1}. As soon as the instrument acquires the Sun in the lower atmosphere, the initiation of a sunrise event, the IFOV is centered along the radiometric

center of the solar image and the scan mirror will move up and down to provide vertical scanning of a solar disk. The scanning motion continues until the tangent altitude reaches 300 km. Figure 3.1.3 shows an example of the measured radiance (expressed in counts) for a SAM II 1000 nm event. The scans are alternately upscans and downscans following solar acquisition. Note the peak intensity of each scan gradually increases until it is constant after approximately 40 s, indicating that the Sun is above the atmosphere. In this example, the attenuation in the lower atmosphere is dominated by Rayleigh and aerosol scattering.

The occultation technique is unique in that the measurement coverage, both spatial and temporal, is strongly linked to the orbit parameters of the spacecraft. With one of the prime scientific objectives being the determination and monitoring of trends in atmospheric constituents, SAGE III must be deployed in a fashion which yields adequate spatial (latitudinal) and temporal (seasonal) coverage. The current planned implementation for SAGE III is to place one instrument in a sun-synchronous orbit and another, concurrently, in a mid-inclination orbit. The addition of a second occultation target, the Moon, increases the sampling and offers complementary coverage, for example, the ability to make measurements during the polar winter night where sunrises and sunsets do not occur.

The spectral variation of atmospheric extinction is illustrated in Figure 3.1.4 showing the contribution of atmospheric extinction versus wavelength from the different constituents at an altitude of 18 km. Both aerosol and Rayleigh scattering contribute at all wavelengths. Ozone has strong absorption in the Hartley-Huggins band (UV) and the Chappuis band in the visible. NO_2 absorbs between 350 and 600 nm. Water vapor has absorption lines throughout the visible, but with a strong band near 940 nm. Although not shown on Figure 3.1.4, NO_3 has absorption features between 500 and 650 nm, and OClO has a strong band at 380-420 nm. SAGE III utilizes the spectrometer with the CCD detector to provide spectral measurements over the wavelength ranges from 280 to 1040 nm so that all of these gaseous species can be detected. An additional channel at 1550 nm is used for near IR aerosol extinction measurements. While SAGE III makes 809 individual spectral measurements, in practice only about 85 discrete values (combinations of 1 or more digitized CCD element measurements) will be routinely transmitted to the ground. These are sufficient to retrieve all gaseous species and aerosol parameters.

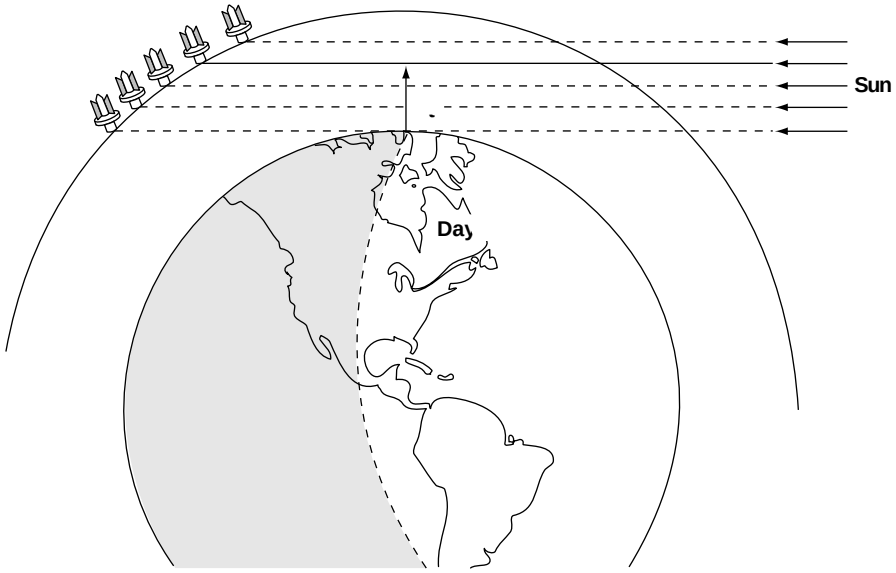

Figure 3.1.1 SAGE III solar occultation measurement geometry. The tangent altitude is denoted by Z_t.

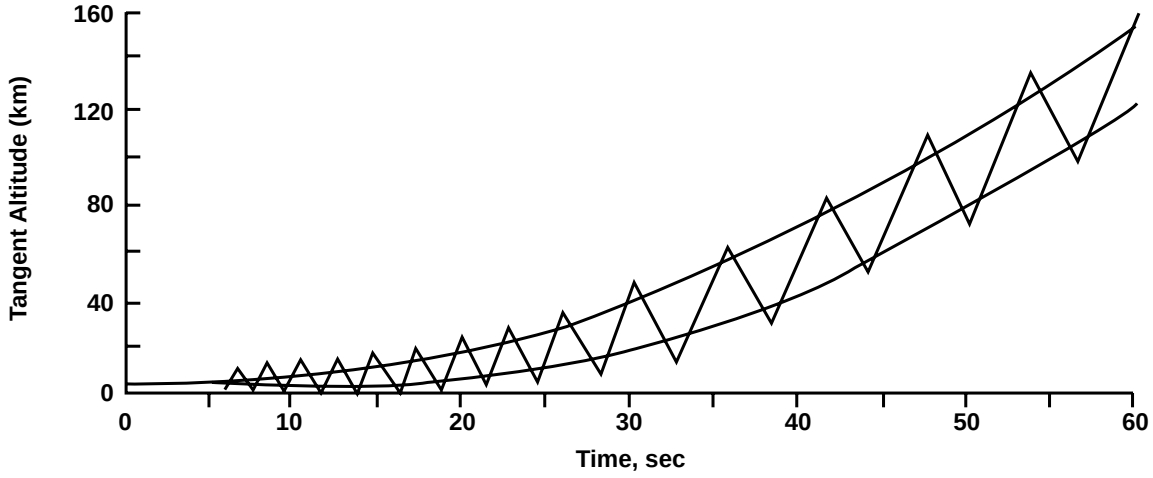

Figure 3.1.2 Typical sunrise event: lines indicate position of top and bottom of the Sun, and scan motion of SAGE III scan mirror across the solar disk.

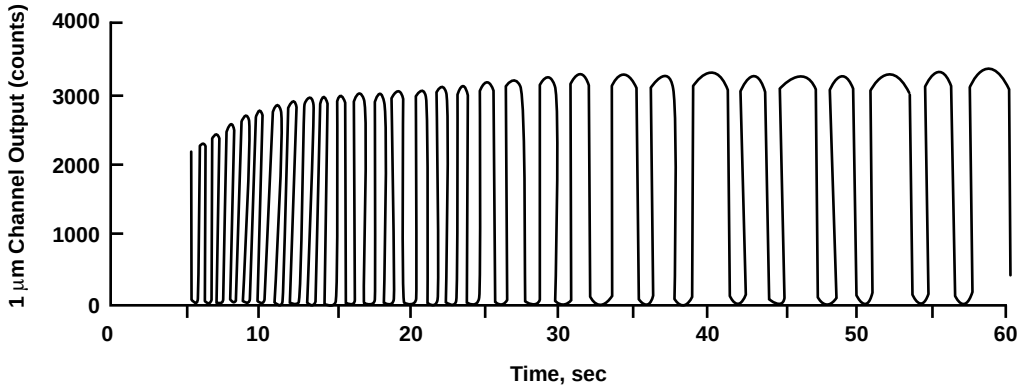

Figure 3.1.3 An example of 1000 nm extinction from SAM II during a sunrise event.

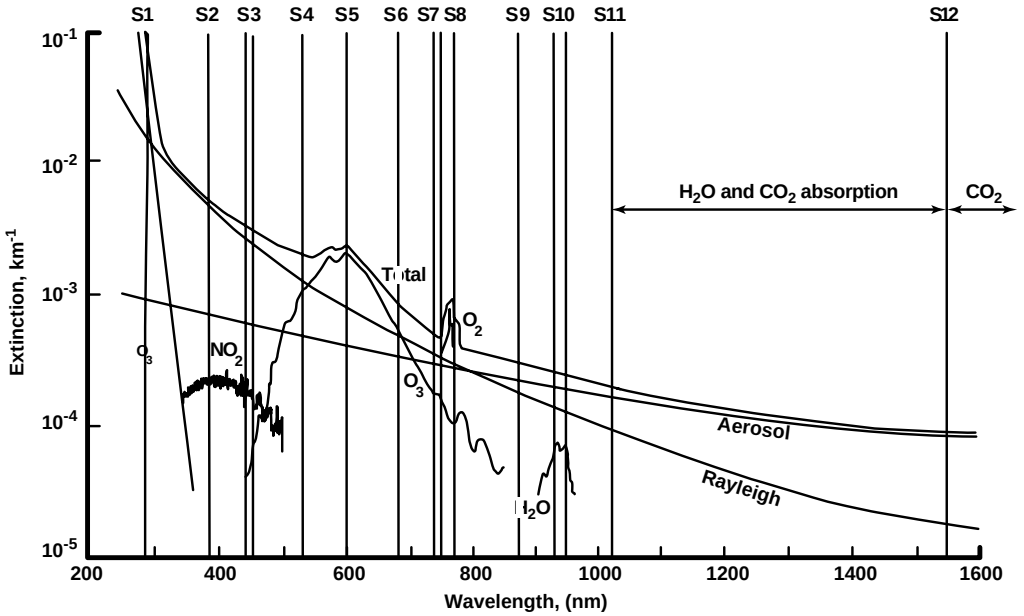

Figure 3.1.4 Wavelength dependence of atmospheric extinction at 18 km (NO_3 and OClO are not shown).

3.1.2 The Forward Problem

The equation of radiative transfer in one dimension for radiance, $I(\lambda, x)$, at wavelength λ, at an arbitrary point x is given by

$$\frac{dI(\lambda, x)}{d\tau(\lambda, x)} = S(\lambda, x) - I(\lambda, x), \tag{3.1.1}$$

where S is the source function and $d\tau(\lambda,x)$ is the optical depth between points x and $x+dx$. The optical depth per unit distance $(d\tau(\lambda,x)/dx)$ is commonly referred to as extinction. The source function consists of contributions from both single and multiple scattering as well as emission. For SAGE III measurements, wavelengths, and geometry (directly observing the Sun through a small IFOV), scattering and emission terms are very small relative to the directly transmitted component and can be ignored. Therefore, Equation (3.1.1) can be simplified to

$$\frac{dI(\lambda,x)}{d\tau(\lambda,x)} = -I(\lambda,x). \tag{3.1.2}$$

The solution to this equation, when the unattenuated radiance (at x=0) is given by $I(\lambda,0)$, is given by

$$I(\lambda,x) = I(\lambda,0)e^{-\tau(\lambda,x)}. \tag{3.1.3}$$

Then, the irradiance, R_N as measured by SAGE III for channel "N", can be expressed as

$$R_N(Z_t) = \int_{\Delta\lambda} d\lambda \int_{\Delta\Omega} d\Omega I(\lambda,0)e^{-\tau(\lambda,Z_t)} W(\Omega)\Psi(\lambda), \tag{3.1.4}$$

where $\tau(\lambda,Z_t)$ is the optical depth along the line of sight at tangent height Z_t between the instrument and the Sun, $\Delta\lambda$ is the spectral width of channel N with band pass function $\Psi(\lambda),\Delta\Omega$ is the angular field of view of the instrument with response $W(\Omega)$. The value of $\tau(\lambda,Z_t)$ varies with tangent altitude; it is effectively 0 above 100 km and generally increases downward. It is composed of contributions from Rayleigh, aerosol, and gaseous species extinction. Transmission along the line of sight, $T_N(Z_t)$ (also called the slant path transmission), at tangent height Z_t, is defined as

$$T_N(Z_t) = R_N(Z_t)/R_N(Z_t^*), \tag{3.1.5}$$

where (Z_t^*) is a tangent altitude well above the atmosphere (> 100 km).

3.2 Retrieval Algorithm Description

3.2.1 Overview and Assumptions

In as much as SAGE III is a fourth generation instrument, the operational software also represents a fourth level in the complexity of the species separation algorithm. The earliest instrument, the Stratospheric Aerosol Measurement (SAM II) (1978-1994) was a single channel (or wavelength) instrument where external Rayleigh or molecular scattering effects were subtracted from the line of sight optical depths. Subsequently, the remaining optical depth peeled to a vertical profile of aerosol extinction at 1000 nm. The

first Stratospheric Aerosol and Gas Experiment (SAGE) (1979-1981), and its follow-on mission SAGE II (1984-present), used measurements (often referred to as "channels") of atmospheric line-of-sight transmission at multiple wavelengths (four and seven, respectively) from the ultraviolet to the near-infrared. These extra channels were employed to infer vertical profiles of multi-wavelength aerosol extinction, ozone (O_3), nitrogen dioxide (NO_2), and, in the case of SAGE II, water vapor (H_2O). These instruments also introduced a new challenge: separating the effects of different species when they affect transmission at more than one measurement wavelength [Chu *et al*., 1989]. While these experiments were highly successful, the extent of mutual interference limited the vertical domain and the accuracy of each species retrieved.

For solar occultation events, SAGE III uses 87 channels between 290 and 1540 nm at which vertical profiles of transmission are determined. This data is used to produce profiles of the molecular density of O_3, NO_2, H_2O, aerosol extinction at 9 wavelengths, cloud presence, temperature, and pressure. With this resolution in the spectral density of the channels, the inversion algorithm has been designed to minimize past difficulties with species separation and improve both the accuracy and vertical range of the data products. In addition, it adds new aerosol extinction channels (at 9 wavelengths), formalizes cloud presence as a data product, and temperature and pressure profiling through the use of the oxygen A-band located near 765 nm. The process or algorithm that leads from raw instrument counts to data products can be broken into two distinct parts: the transmission algorithm and the species inversion algorithm. The different steps in the transmission and inversion algorithms and the overall flow of the algorithm are illustrated in Figure 3.2.1. Details of the transmission algorithm may be found in the SAGE III Transmission ATBD (LaRC475-00-108). A brief overview of the transmission algorithm follows. The species-inversion algorithm overview is discussed in Section 3.2.2. The species-specific segments of the algorithm are in following sections.

Transmission Algorithm Summary

The function of the transmission algorithm is to produce multi-wavelength slant path transmission profiles from time sequences of radiometric and engineering measurements by the SAGE III instrument. As shown in Figure 3.2.1, this process can be separated into five components: data screening, position registration, altitude registration, wavelength registration, and data grouping and statistics. The first step in the transmission algorithm is the screening of the input level zero (telemetry) data. The data-screening algorithm locates missing or bad data and determines whether the data are recoverable. Next, the position registration algorithm determines solar point positioning and the tangent height. The tangent height is the altitude at which the ray is closest to the Earth's surface for the line-of-sight that originates from the center of the instrument's field of view to the position on the sun. Taking the ratio of the science scan data (any data with an associated tangent height below 100 km) relative to the same solar position on exoatmospheric scans produces atmospheric transmission for an individual measurement. The tangent height

calculation provides the height registration of the derived transmission values. Generally, tangent height is dominated by geometric concerns, however it is corrected for atmospheric refraction, which becomes increasing significant below 30 km. Each channel is also calibrated for wavelength using an operation mode of the instrument that occurs at tangent altitudes well above normal operation regions in the atmosphere. Using all 809 pixels, a multi-linear regression procedure is used to assign spectral positions to individual pixels by using a standard solar spectrum (Limitations in the availability of on-board storage prohibit downlinking all 809 elements of the CCD array for each occulation event). The solar spectrum has complex spectral features including the solar Fraunhofer lines that measured by the SAGE III CCD spectrometer system. In this manner, shifting and stretching of the pixels on the CCD device due to thermal or mechanical perturbations can be accounted for and the center wavelength for each of the 809 pixels will be accurately determined. The final step in the transmission algorithm is the data grouping and statistics. This procedure takes the individual transmission data (up to several thousand data points per channel) into altitude profiles and performs statistical analyses to determine the characteristics of the distribution of the measured data in each group. Transmission profiles for each channel are produced on a 0.5-km grid from 0.5 km to 100 km with an uncertainty estimate. The correlation between channels at 521, 1020 and 1540 nm at altitudes between 6.5 and 26.5 km is also calculated as required input to the cloud presence algorithm.

3.2.2 Species Separation Algorithm

The species separation algorithm involves the inversion of the multi-wavelength slant path transmission profiles into vertical profiles of the molecular density of SAGE III-measured gas species as well as aerosol extinction at several wavelengths between 290 nm and 1550 nm. For most species the inversion algorithm works with the slant path optical depth, $\tau_\lambda(z_t)$, rather than directly with the transmission profile $T_\lambda(z_t)$, which can be expressed for wavelength, λ, and slant path tangent height, z_t, as

$$\tau_\lambda(z_t) = -In(T_\lambda(z_t)) \ . \tag{3.2.1}$$

The slant path optical depth at each SAGE III measurement wavelength consists of several components including molecular or Rayleigh scattering, aerosol extinction, and usually absorption by one or more gaseous species. At each tangent height, SAGE III will make measurements at 87 wavelengths (or channels) between 290 nm and 1540 nm distributed as shown in Table 3.2.1. The ensemble of SAGE III measurements at a given tangent height can be expressed as a series of linear equations of the form

$$\tau_\lambda = \tau_{\lambda R} + \tau_{\lambda a} + \sum_{n=1}^{N} \tau_{\lambda gn}, \tag{3.2.2}$$

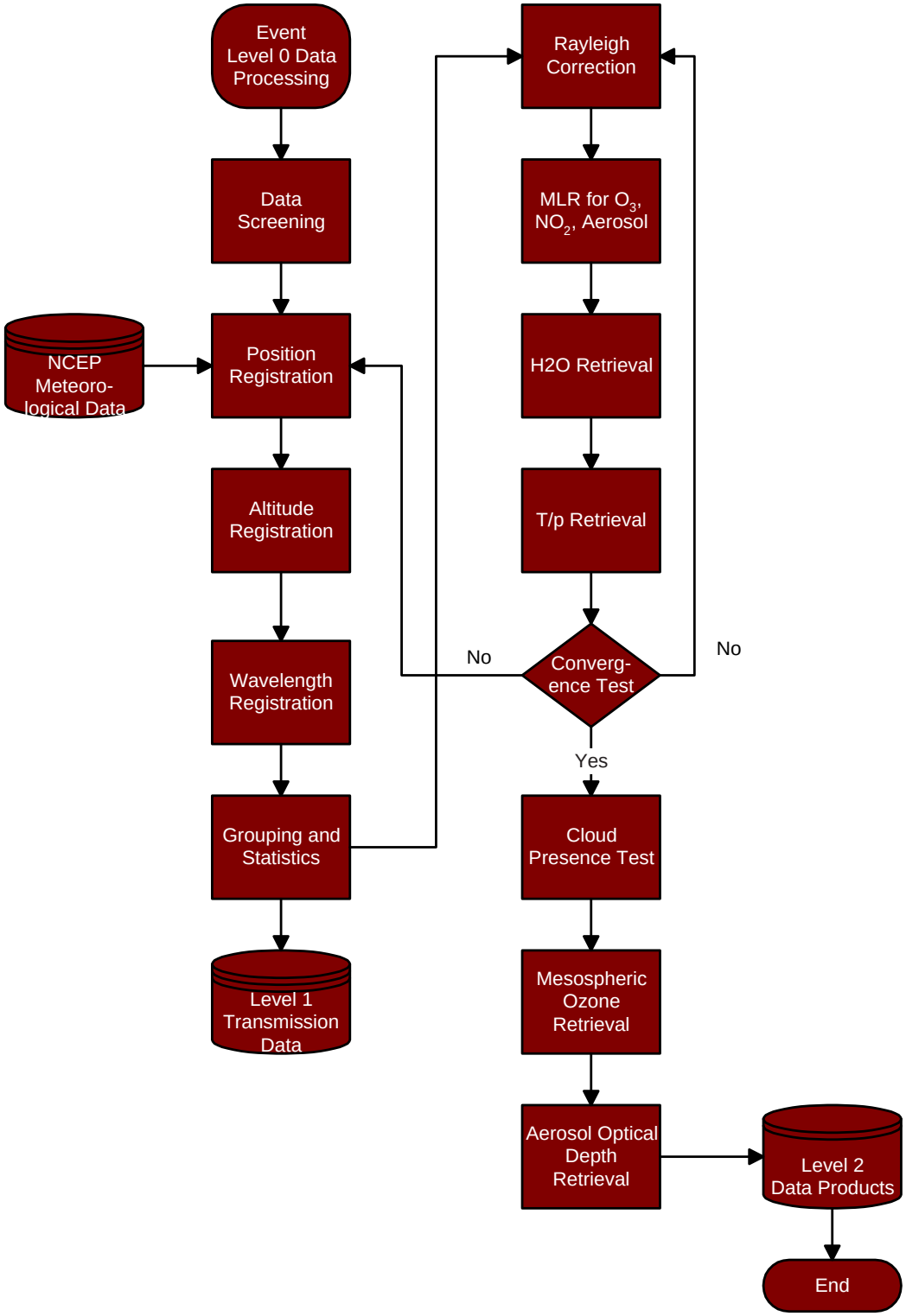

Figure 3.2.1 Flow of data through the SAGE III processing algorithm.

where $\tau_{\lambda R}$ is the Rayleigh slant path optical depth, $\tau_{\lambda a}$ is the aerosol slant path optical depth, and $\tau_{\lambda gn}$ is the slant path optical depth for gas species n, where N can be from 0 to 4. A crucial element of the inversion process is the partitioning of the total slant path optical depth at each wavelength and tangent altitude into the contributions of the individual components. Thus, for the measurement ensemble, there are unknown molecular and aerosol components at each wavelength, unknown temperature and pressure, as well as unknown ozone, nitrogen dioxide, and water vapor molecular densities, or, in a nominal sense, more than twice as many unknown parameters as measurements at each tangent altitude. Table 3.2.1 lists the primary and interfering species for each channel.

Table 3.2.1 SAGE III channel groupings with primary and interfering species.

Channel Grouping		**Primary Species**	**Interfering Species**+
S1	290 nm	O_3	
S2	385 nm	Aerosol	NO_2, O_3
S3	433-450 nm	NO_2, Aerosol	O_3
S4	521 nm	Aerosol, Cloud	NO_2, O_3
S5	563-622 nm	O_3, Aerosol	NO_2, H_2O
S6	676 nm	Aerosol	O_3
S7	758 nm	Aerosol	O_3
S8	759-771 nm	O_2 (T,p)	O_3
S9	869 nm	Aerosol	O_3, H_2O
S10	933-960 nm	H_2O	O_3
S11	1020 nm	Aerosol, Cloud	O_3
S12	1540 nm	Aerosol, Cloud	CO_2, H_2O

+ Any species influencing the retrieval of the primary species except the omnipresent Rayleigh and aerosol components.

The Rayleigh contribution has a well-known wavelength dependence (λ^{-4}) and is dependent only on the total molecular mass along the slant path. Formally, this can be expressed as

$$\tau_{\lambda R} = \int_{z_t}^{\infty} \sigma_{\lambda R} \rho(z) dx_{\lambda}(z, z_t), \tag{3.2.3}$$

where $\sigma_{\lambda R}$ is the Rayleigh mass extinction coefficient determined using the formulation of Bucholz [1996]. In this equation, $\rho(z)$ is the molecular mass density as a function of height and determined from the current values for the temperature and pressure profiles

and the ideal gas law, and $dx_\lambda(z,z_t)$ is the length of the slant path between the altitudes of z and $z+dz$ and includes the effects of spherical geometry and wavelength-dependent refraction [Chu, 1983]. Like the refraction component of the transmission algorithm, the unknown Rayleigh slant path optical depth is initially estimated using temperature and pressure profiles supplied by the NCEP and the GRAM 95 climatology (for altitudes above 50 km) [Justus *et al.,* 1995]. A branch back to either the refraction module or the Rayleigh calculation may be required if the difference between the final temperature and pressure product and the initial guess is sufficiently large.

The next step in the inversion process is to derive slant path number density profiles for NO_2 and O_3 using multiple linear regression (MLR) and the channels for these species listed in Table 3.2.1 (S3 and S5). The advantage of this procedure is that the fine structure of these species, particularly NO_2, permits the extraction of the column densities independently of either the aerosol or molecular components. It is necessary to simultaneously solve for these species since they absorb significantly in both spectral regions (433-450 nm and 562-622 nm). The MLR inversion process is discussed in detail in Section 3.2.3. Once the slant-path column densities have been derived, the influence of NO_2 and O_3 is removed from all measurement wavelengths in which it is a component excluding the mesospheric ozone channel at 290 nm. The slant path aerosol optical depths for the nominal SAGE III aerosol channels at 385, 448, 521, 595, 676, 758, 869, 1020, and 1540 nm (involving S2-S7, S9, S11 and S12). They are retrieved as residuals of the MLR retrievals of O_3 and NO_2 and thus are effectively a part of the MLR procedure.

In both the center of the ozone Chappuis band and in some of the aerosol channels, water vapor is a minor contributor that cannot be initially corrected. Thus, in the first iteration, the water vapor correction in these channels will be neglected. While, for subsequent iterations, it will be determined using the current retrieved water vapor profile using the method described in Section 3.2.4.

The next stage in the retrieval process is the retrieval of the water vapor profile. Since both aerosol and ozone significantly contribute in the SAGE III water vapor channels between 933 and 960 nm (Table 3.2.1), the first step in the water vapor retrieval algorithm is to isolate the water vapor contribution. The effects of ozone can be estimated using the MLR ozone product and the appropriate cross sections. For aerosols, we have initially implemented a simple multi-channel interpolation to remove the influence of aerosol using the aerosol derived as a part of the MLR procedure. This is similar to the approach used with earlier SAGE inversions; however, the increase in number and proximity of aerosol channels greatly improves this approach and modeling indicates that this is sufficient for most circumstances. However, more robust approaches are under investigation that allow the retrieval to estimate the water vapor profile, aerosol, and ozone effects independently of estimates of aerosol and ozone based on measurements at other wavelengths. This may be particularly advantageous for ozone effects since the

temperature dependence of ozone absorption in the water vapor feature is not well known and the magnitude of ozone absorption may exceed that of water vapor at some altitudes. With the current method, given the profile of water vapor slant path optical depths, the vertical profile of water vapor density is solved for using the procedure described in Section 3.2.4. It is a standard Levenberg-Marquardt inversion that, unlike aerosol, O_3, and NO_2 (which remain in slant path format at this point of the inversion process), directly produces a vertical profile of water vapor molecular density. The derived water vapor profile may be used on subsequent iterations to remove the influence of water outside the nominal water vapor band. In particular, water vapor absorbs weakly near 600 nm (and thus influences ozone retrievals) as well as at 869 nm (influencing the aerosol extinction measurement at that wavelength).

The next stage in the retrieval process is the retrieval of temperature and pressure (T/p). Water vapor, aerosol and ozone contribute in a generally small but significant way to the total optical depth in the SAGE III O_2 A-Band channels between 759 and 771 nm (Table 3.2.1). As with the water vapor retrieval, we have initially implemented a simple multi-channel interpolation to remove the influence of aerosol using the aerosol slant path optical depth derived as a part of the MLR procedure. In addition, the effects of ozone can be estimated using the MLR ozone product and the appropriate cross sections. Once those species have been accounted for, the residual values are the slant path oxygen A-band optical depths. Given the profile of oxygen A-band slant path optical depths (at 14 channels), the vertical profiles of temperature and pressure are determined using a non-linear Marquardt-Levenberg method described in Section 3.2.5. Like the water vapor inversion algorithm, the T/p procedure yields vertical profiles rather than slant path profiles.

Both the water vapor and the temperature and pressure retrieval algorithms require a forward model as part of the retrieval process. We have implemented the Emissivity Curve-of-Growth Approximation (EGA), which is described an Appendix B. Testing suggests that it is adequate and far quicker than line-by-line calculations.

At this point of the retrieval process, it is possible that branching backward in the retrieval process is possible. While unlikely, it is possible that the change in atmospheric density (as inferred by the T/p retrieval) could be sufficiently large to change altitude registration performed in the transmission section of the retrieval process. In this case, the processing branches back to the refraction computation segment of the transmission calculation. It is also possible that the processing could branch back to the Rayleigh optical depth or water vapor sections of the species separation algorithm if the change in the estimated Rayleigh correction profile exceeds the estimated uncertainty in those profiles. Otherwise, the processing branches to the final stages of the inversion process. The branching process will be a run-time controllable feature.

The final stages of the retrieval algorithm are mesospheric ozone retrieval, profile peeling, cloud presence detection, and aerosol stratospheric optical depth calculation. The mesospheric ozone algorithm makes use of the 290 and 385 nm line-of-sight optical depths (uncorrected for Rayleigh). Profile peeling (the conversion from line-of-sight or slant path optical depth to extinction profile or number density) follows the SAGE II processing method in which a modified-Chahine method [Chahine, 1972; Twomey, 1975; Chu and McCormick, 1979; Chu, 1985; Chu *et al.,* 1989] was employed, though alternative methods are available as runtime selectable options, including simple onion peeling.

The algorithm for detecting cloud presence, a level 3 product, is described in a separate document (SAGE III Cloud ATDB, LaRC475-00-106). The basic algorithm relies upon wavelength ratios between the aerosol extinctions in these channels (clouds tend to be "white") and it also requires a separate user driven quality control process for which a separate document is being developed.

With all species transformed to vertical profiles, construction of the data products listed in Table 1.6.1 is executed and the data is made available for archival.

Uncertainty Estimation

Satellite measurements contain uncertainty that includes both random and systematic components. As in the SAGE and SAGE II retrievals, the SAGE III measurements will provide uncertainty estimates for random components [Russell *et. al.,* 1981; Chu *et. al.,* 1993]. In the case of systematic uncertainty, it is normally secondary and can be assessed through sensitivity analysis. There are three primary sources of the random component of the uncertainty: (a) line-of-sight optical depth measurement errors, (b) the Rayleigh optical depth estimate, and (c) uncertainties resulting from the removal of contributions by interfering species. The basic concept of the reported SAGE III data-products uncertainties is the transference of measurement error to data product error via the mathematical processes that produce them.

The grouping and statistics algorithm described in the SAGE III Transmission ATDB determines errors in the line-of-sight optical depth (or its companion transmission). The measurement error can be modified by the removal or clearing of the species which are considered to "interfere" with the retrieval process. This usually includes the Rayleigh component and, in some cases, one or more data products such as the removal of ozone from the water vapor and temperature/pressure channels. If branching back occurs, the Rayleigh uncertainty would be modified and water vapor uncertainty included at the appropriate channels. This modified error then becomes the base measurement error.
The method by which these uncertainties propagate into species is greatly dependent on the method employed. For instance, MLR error in the line-of-sight values is a product of

the MLR mathematical process measurement spectrum and not strongly dependent on the estimated signal error. This is described in more detail in Section 3.2.3 and in common reference material [e.g., Bevington, 1969]. Since aerosol is predominately a residual of the MLR process its error is dominated by the measurement error and the species errors estimated by this algorithm.

To propagate errors determined for line-of-sight quantities (O_3, NO_2, NO_3, OClO, and aerosol) to the uncertainties in the vertical profile is a straightforward application of the least-squares form of onion peeling. The vertical profile of measurement variance (a vector, $\underline{q}$) (uncertainty squared) is multiplied by the inverse of the path length matrix, P to produce the data product variance which can be expressed as

$$\underline{g} = P^{-1}\underline{q}$$

An element of the limb path length matrix contains the physical distance traversed by the line-of-sight ray path for a tangent layer n through layer m (non-zero only for $m \geq n$).

In the Marquardt-Levenberg method, (used by water vapor and T/p retrieval algorithms), covariance matrices are produced that translate measurement error into species uncertainties. In this case, since the products of these algorithms are the final data products no further modification of the estimated error is required.

Table 3.2.2 Uncertainty estimates

Species	**Expected Precision**	**Altitude Range**
Aerosol 1020 nm, 521 nm	5%	0-40
Temperature	2 K	0-85
Pressure	2%	0-85
Ozone (Solar)	5%	5-85
Ozone (Lunar)	<10%	15-35
Nitrogen Dioxide (Solar)	15%	10-50
Nitrogen Dioxide (Lunar)	15%	20-35
Water Vapor	15%	0-40
Chlorine Dioxide	20%*	15-25
Nitrogen Trioxide	10%	20-50

*Under enhanced condition.

Note that systematic sources of error are neglected in the discussion above. These arise primarily due to the degree to which basic physical assumptions are obeyed (e.g., spherical homogeneity; see Appendix C), imperfect knowledge of instrument performance, spacecraft ephemeris, and spectroscopy. An assessment of the current state of spectroscopy as it relates to SAGE III is given in Appendix D.

3.2.3 Ozone / Nitrogen Dioxide / Aerosol Retrieval

Slant path number density profiles for O_3 and NO_2 are derived using multiple linear regression (MLR) for channels S3 and S5. MLR simultaneously solves for O_3 and NO_2, which absorb significantly in both spectral regions (433-450 nm and 563-622 nm), independently of aerosol and molecular components. Aerosol contribution is derived as a residual at 9 wavelengths.

Multiple Linear Regression

The SAGE III slant path optical depth measurement at a tangent height, for Ozone and NO_2 channels (S3 and S5) can be expressed, after removing the Rayleigh slant path optical depth, as

$$\tau(\lambda_i) = n_{O_3}\sigma_i(\lambda_i, O_3) + n_{NO_2}\sigma_i(\lambda_i, NO_2) \tag{3.2.4}$$

or

$$\tau(\lambda_i) = \sum_k n_k \sigma_{ki}(\lambda_i). \tag{3.2.5}$$

Alternatively, $\tau(\lambda_i)$ may be expressed in matrix form as

$$\begin{bmatrix} \tau_{433} \\ \tau_{434} \\ . \\ . \\ \tau_{450} \end{bmatrix} = \begin{bmatrix} \sigma_{433}(O_3) & \sigma_{433}(NO_2) \\ \sigma_{434}(O_3) & \sigma_{434}(NO_2) \\ \cdots & \cdots \\ \cdots & \cdots \\ \sigma_{450}(O_3) & \sigma_{450}(NO_2) \end{bmatrix} \begin{bmatrix} n_{O_3} \\ n_{NO_2} \end{bmatrix} \tag{3.2.6}$$

or

$$T = SN, \tag{3.2.7}$$

where T is the measurement vector (N dimensional vector), N is the unknown species or solution vector (M dimensional), and S is the matrix relating the two vectors ($N \times M$ dimensional matrix) through their differential absorption spectra. The normal equations have the form

$$\sum_{i=1}^{N} \frac{\tau_i \sigma_k(\lambda_i)}{\varepsilon_i^2} = \sum_{j=1}^{M} \left[\sum_{i=1}^{N} \frac{\sigma_j(\lambda_i)\sigma_k(\lambda_i)}{\varepsilon_i^2} \right] N_j, \tag{3.2.8}$$

where the uncertainty ε_i has been included explicitly. In matrix form, this expression becomes

$$S^{\mathrm{T}} T = [S^{\mathrm{T}} S] N \tag{3.2.9}$$

with suitable representation of the weighted observations with T, the derived parameters by the vector N, and the normal matrix S. Since this is a well constrained set of equations, the solution to this set of linear equations can be found using a least-squares solution

$$N = [S^{\mathrm{T}} S]^{-1} S^{\mathrm{T}} T \tag{3.2.10}$$

or

$$n_j = \sum_{k=1}^{M} C_{jk} \left[\sum_{i=1}^{N} \frac{\tau_i \sigma_k(\lambda_i)}{\varepsilon_i^2} \right], \tag{3.2.11}$$

with the variance ε^2 of each derived parameter given by

$$\varepsilon^2(n_j) = \sum_{k=1}^{M} \sum_{l=1}^{N} C_{jk} C_{jl} \left[\sum_{i=1}^{N} \frac{\sigma_k(\lambda_i)\sigma_l(\lambda_i)}{\varepsilon_i^2} \right], \tag{3.2.12}$$

where the covariance-correlation matrix $C \equiv [S^T S]^{-1}$. The diagonal elements of C are the variances of the fitted parameters, and the off-diagonal elements are the covariance between species.

After the initial column density computation, the absorption contribution by a species may be removed by multiplying the column density value by the absorption cross section and subtracting from the ratio data.

Aerosol slant path optical depth is retrieved as a residual of the MLR retrievals of O_3 and NO_2 and thus is effectively a part of the MLR procedure. If the algorithm branches back and water vapor data is available, some channels are corrected for water vapor particularly at 869 and 1540 nm (which is also cleared for absorption by carbon dioxide).

The uncertainty in the slant path aerosol values, σ_{aer}, is calculated based on measurement error, σ_m, and errors associated with the removal of interfering species, $\sigma_{species}$, or

$$\sigma_{aer}^2 = \sigma_m^2 - \sum \sigma_{species}^2 . \tag{3.2.13}$$

For all nine channels this includes at least Rayleigh but also generally includes the effects of at least one other species including O_3, NO_2, H_2O, and CO_2 (which is estimated from the temperature and pressure profile for the 1540 nm channel).

Aerosol slant path optical depth estimates in the temperature and pressure channels (S8) and water vapor channels (S10) are accomplished using Lagrangian interpolation [e.g., Stark, 1970] using nearby aerosol channels. This method, when compared to more physically based methods, yields similar results. Current research on both the temperature/pressure retrieval and water vapor retrieval will ultimately make this function unnecessary. Figure 3.2.2 and Figure 3.2.3 are examples of simulated retrieval and absolute error of O_3, NO_2 and aerosol (channels 521 and 1020 nm) slant path optical depth.

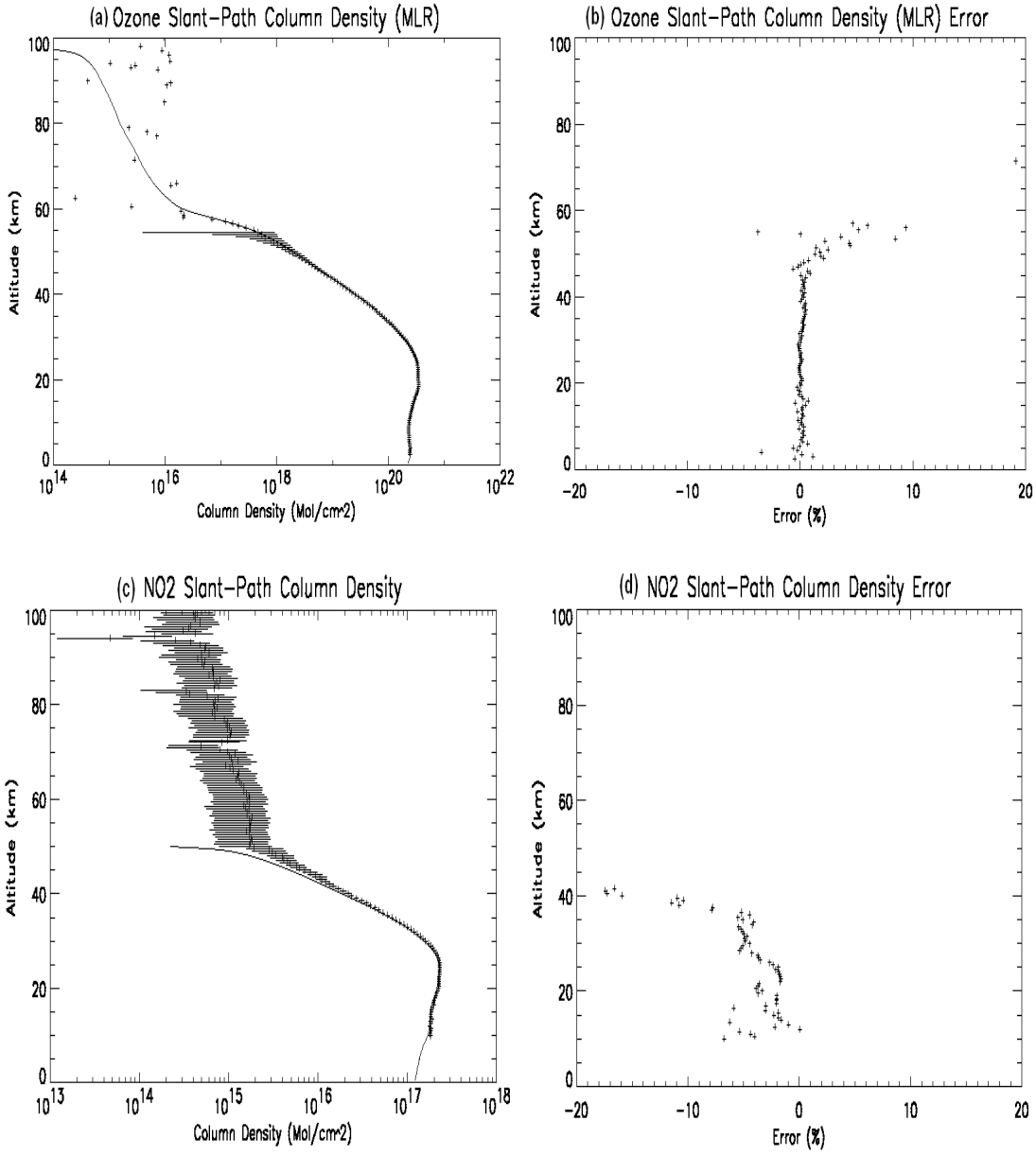

Figure 3.2.2 Simulated retrieval and absolute error of O_3 and NO_2 Slant path column density.

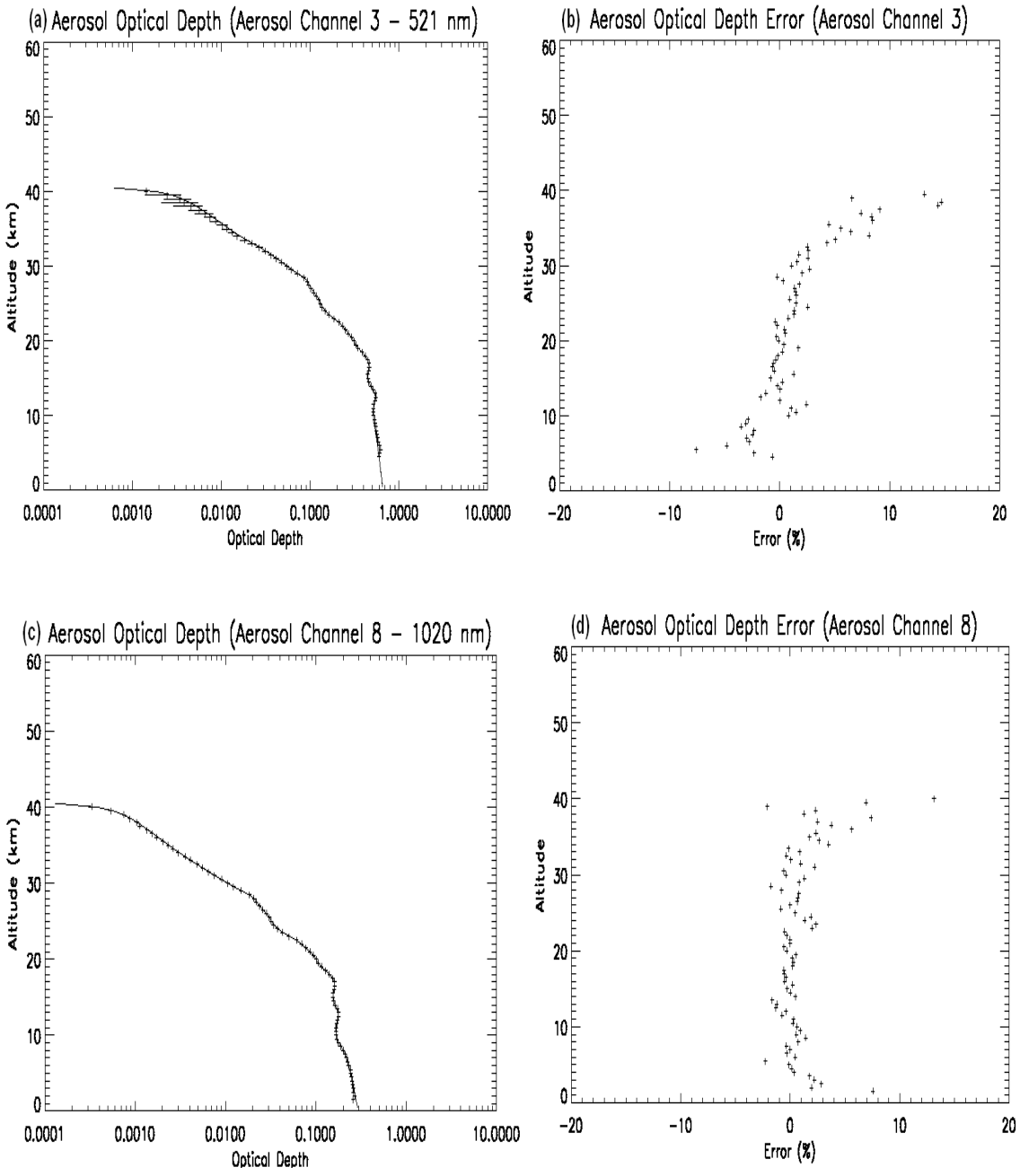

Figure 3.2.3 Simulated retrieval and absolute error of aerosol slant path optical depth at 521 and 1020 nm.

3.2.4 Water Vapor Retrieval

Water vapor measurement from the SAGE III instrument is accomplished through the limb extinction measurements at the 940 nm wavelength region with twenty nine channels of spectral bandpass of about 2 nm located from 930 nm to 960 nm centered at the $\rho\sigma\tau$ band of water vapor. These spectral measurements provide both redundant measurements of the water vapor absorption and a good discrimination of absorption signatures from other species such as ozone and aerosol. A detailed discussion of the important parameters involved in the SAGE III water vapor measurement and retrieval process is presented here.

Because the interference due to air molecules, aerosols, and ozone, Equation (3.2.2), which describes the SAGE III slant path optical depth measurement at a tangent height z_t, for water vapor channels can be explicitly expressed as

$$\tau_\lambda(z_t) = \tau_{\lambda H_2O}(z_t) + \tau_{\lambda R}(z_t) + \tau_{\lambda a}(z_t) + \tau_{\lambda O_3}(z_t) \tag{3.2.14}$$

where $\tau_{\lambda H_2O}$ is the water vapor slant path optical depth, $\tau_{\lambda R}$ is the Rayleigh slant path optical depth, Equation (3.2.3), $\tau_{\lambda a}$ is the aerosol slant path optical depth, and $\tau_{\lambda O_3}$ is the ozone slant path optical depth. As discussed in Inversion Algorithm (Section 3.2.2), the Rayleigh slant path optical depth is estimated from the temperature and pressure profile possibly derived using the SAGE III oxygen A-band measurements (759-771 nm) described in Section 3.2.5. The removal of ozone interference is straightforward by incorporating the retrieved ozone number density profile (Section 3.2.3) together with ozone spectral information at water vapor wavelengths.

Next, aerosol extinction at each water vapor channel is estimated (and removed) using a simple Lagrangian interpolating polynomial and the nearby aerosol values previously derived for 670, 758, 869, and 1020 nm. The residual optical depth is the water vapor slant path optical depth ($\tau_{\lambda H_2O}(z_t)$).

The EGA (Emissivity Growth Approximation) approach has been adopted for the forward model calculation of the slant path transmission for water vapor. The emissivity growth approximation (EGA) [Gordley and Russell, 1980] has been shown to be sufficiently accurate and rapid to permit routine computation of the water vapor transmission profiles in the 940 nm wavelength region [Chu *et al*., 1993]. The technique currently adopted for the SAGE III retrieval of water vapor is a global fit approach similar to the method described by Carlotti [1988]. The global fit method uses a non-linear least squares procedure to simultaneously fit absorption measurements from all spectral channels and slant paths. In this approach, we evaluate a χ^2 merit function and search for a set of water vapor mixing ratios which minimize it. The χ^2 merit function is defined as

$$\chi^2(H_2O) = \sum_{j=1}^{M}\sum_{i=1}^{N}\left[\frac{A_j^m(\lambda_i) - A_j^c(\lambda_i; H_2O)}{\sigma_{ij}}\right]^2 \qquad (3.2.15)$$

where $A_j^m(\lambda_i)$ are the measured H_2O absorption values (corrected for Rayleigh, aerosol, and ozone) for slant path *j* and subchannel *i*; $A_j^c(\lambda_i; H_2O)$ are the computed absorption values for slanth path *j* and subchannel *i*; *M* is the number of tangent heights; and *N* is the number of subchannels. The computed absorption $A_j^c(\lambda_i; H_2O)$, are interpolated from a database of slant path absorptions generated using line-by-line calculations and the pseudo mass path approximation [Gordley and Russell, 1980].

The global fitting algorithm employs the Marquardt method [Marquardt, 1963] to perform the non-linear least squares fit. The Marquardt method, a well known procedure that has become a standard of non-linear least squares routines, minimizes the merit function using an iterative procedure that has the advantage of alternating between the inverse-Hessian method and the steepest descent method as appropriate. Functionally, the retrieval using the Marquardt method proceeds as follows:

(1) the merit function $\chi^2(H_2O)$ is initially calculated using the first-guess H_2O profile;

(2) the H_2O mixing ratios are adjusted using either the inverse-Hessian or steepest descent method as appropriate and a new merit function, $\chi^2(H_2O + \delta H_2O)$, is calculated;

(3) the difference between the old and new merit functions, $\chi^2(H_2O) - \chi^2(H_2O + \delta H_2O)$, is calculated;

(4) steps (2)-(3) are repeated until the convergence criteria have been met [typically defined as when the magnitude of $\chi^2(H_2O) - \chi^2(H_2O + \delta H_2O)$ is less than a preset value (~1%)]. The propagation of measurement (random) uncertainty to uncertainty in the water vapor profile is a by-product of the Marquardt procedure that produces a covariance matrix.

Figure 3.2.4(a) illustrates the spectral variation of the water vapor transmission signal at 10 km tangent altitude. The small scale structure in this figure shows the sensitivity of the measured absorption to channel location. The measurements obtained from SAGE III instrument will allow us to over sample the spectra with 29 sub-channels equally spaced at intervals of approximately 1 nm.

We have performed several simulated retrievals using the above-mentioned approach. An illustrative example of a simulated retrieval is shown in Figure 3.2.4(b)-(d). This retrieval was based on simulated water vapor slant path absorption measurements with realistic random noise (signal to noise ratio of 3000). The true (input) water vapor profile [solid line in Figure (b)] is based on a typical mid-latitude profile in the summer. The "first

guess" profile [dotted line in Figure (b)] is also shown. As can be seen, the retrieved profile (symbols "X") reproduces the true water vapor profile extremely well throughout 10 to 40 km.

Above 40 km, the retrieval tends to oscillate about the true profile. The differences (retrieved minus true) expressed in percentage are shown in Figure 3.2.4(c). The results have led to the conclusion that the percentage differences are within 10% for all altitudes below 40 km.

The random component of error in the water vapor retrievals is associated with uncertainties in the residual water vapor slant path absorption values. These uncertainties include both the random noise associated with the SAGE III absorptivity measurements in the 930 - 960 nm wavelength region and the uncertainties involved with removing the Rayleigh scattering, aerosol, and ozone contributions. The dominant component will be due to random noise in the absorption measurements. Figure 3.2.4(d) shows the expected uncertainties as a function of altitudes with signal to noise ratio of 3000. The $1-\sigma$ errors in the retrieved water vapor mixing ratios range from less than 5% in the lower stratosphere and the upper troposphere (below 35 km) to about 10% to 20% in the altitude region 35 to 45 km.

Water Vapor Uncertainty Estimate

Simulation analysis with estimated SAGE III instrument measurement capability indicates an accuracy of 3% to 4% of the retrieved water vapor profile. With the consideration of the uncertainty in the temperature retrieval, altitude registration, and in the removal of contribution due to interfering species, including air molecules, aerosols, and ozone, the total water vapor random uncertainty is about 5% to 15% in the altitude range between 5 and 40 km (Table 3.2.2).

During periods of heavy aerosol loadings, the estimated uncertainty of SAGE III retrieved water vapor concentration will increase significantly. Results of simulated studies indicate that if we assume aerosol optical depths to be 10 times larger than the corresponding values for background level, the random component of error due to removal of aerosol will increase by a factor of 2 to 18 and 1.5 to 12 in the altitude range between 10 and 20km and between 20 and 30 km, respectively.

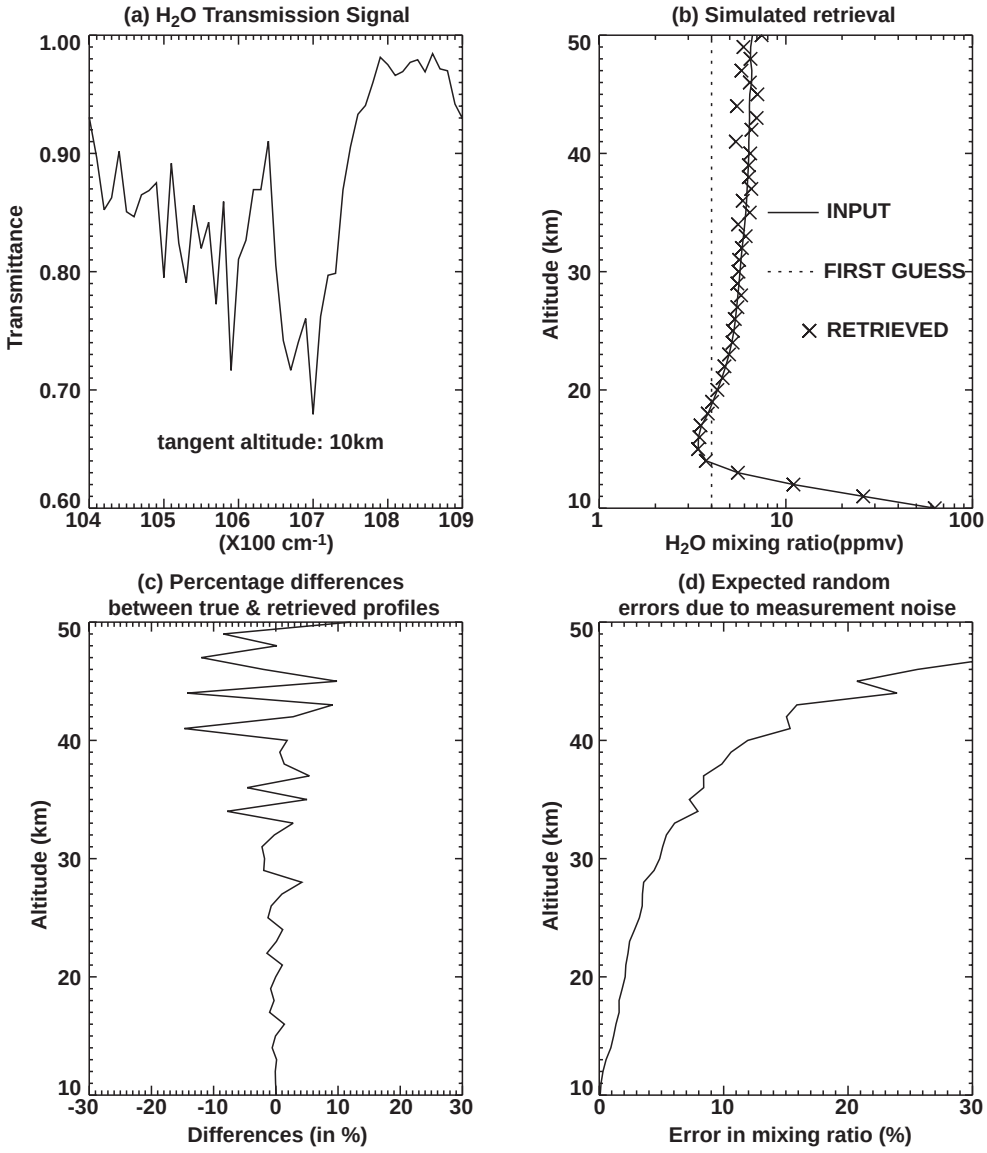

Figure 3.2.4 Examples of H_2O transmission signal and simulated retrieval.

3.2.5 Temperature and Pressure Retrieval

Formulation of the Inverse Problem for Temperature and Pressure Retrieval

The retrieval of temperature and pressure profiles will be performed utilizing the measurements of the oxygen A-band absorption spectrum. The oxygen A-band possesses several features that make it well suited for remote temperature sensing. The line strengths at the center of the absorption band are quite strong; therefore, high signal-to-noise measurements can be obtained at the band center. The number of strong lines in the

band is less than 200; therefore, an accurate analytical computation of the measurement parameters can be performed quite efficiently. In addition to the above features, the temperature dependent parameters for the line strengths vary from positive to negative over the A-band. For example, at wavelengths far away from the band center, the line strength increases with increasing temperature, while at wavelengths close to the band center, the line strength decreases with increasing temperature. This unique sensitivity of the line strength to temperature can be utilized for highly accurate temperature profile sensing. An example of the fine structure present in the oxygen A-band absorption spectrum is shown in Figure 3.2.5.

SAGE III will measure the oxygen A-band spectrum from approximately 759 to 771 nm with a resolution of approximately 1.4 nm (full width at half maximum). The spectrum will be oversampled with 14 channels equally spaced across the spectrum at approximately 1-nm intervals. An example of the oxygen A-band absorption spectrum displayed with the SAGE III spectral resolution is shown in Figure 3.2.6. As illustrated in the figure, the broad features of the A-band are observable at the SAGE III spectral resolution.

In addition to absorption by molecular oxygen, Rayleigh and aerosol scattering and ozone absorption contribute to the extinction over this spectral region (Figure 3.1.4). The Rayleigh scattering component of the A-band measurements is temperature and pressure dependent and will be included in the retrievals. However, the ozone absorption and aerosol scattering components of the A-band measurements possess no useful temperature and pressure information and, as a consequence, it is desirable to remove these "interfering" contributions from the measurements before the retrievals are performed. The ozone optical depth contribution in each of the A-band channels is calculated as the spectrally-integrated product of the ozone number density retrieved from independent SAGE III measurements at wavelengths outside the A-band and the ozone molecular cross sections tabulated for the A-band spectral region. The aerosol slant path optical depth in each of the A-band channels is determined by interpolation from independent SAGE III aerosol slant path optical depth measurements at the four wavelengths: 676, 758, 868, and 1020 nm. It should be emphasized that although the robustness of the temperature and pressure retrievals does not depend on the exact nature of how these corrections are performed, it is dependent on their accuracy. Therefore, it is critical to include the uncertainty associated with these corrections in the total uncertainty calculations for the retrieved parameters.

The magnitude and spectral variation of the A-band absorptivity measurements depend on the atmospheric temperature and pressure distribution in a complicated, non-linear fashion. The accurate retrieval of these parameters requires an inversion technique that will utilize the maximum available spectral information. Various techniques have been tested with differing results. Simulations performed using a standard onion peeling method suggest that temperature and pressure profiles cannot be retrieved with the desired accuracy using this technique. Simulations have also been performed using a global fit approach [Carlotti, 1988], which uses a non-linear least squares procedure to simultaneously fit transmissions from all spectral channels and slant paths. The global fit

method makes use of all the information contained in each measured transmission profile, while the onion-peeling method neglects information below the current tangent altitude. As a result, the global fit approach has demonstrated a higher degree of accuracy than the onion peeling technique and, therefore, we have adopted this approach for performing the SAGE III temperature and pressure retrievals.

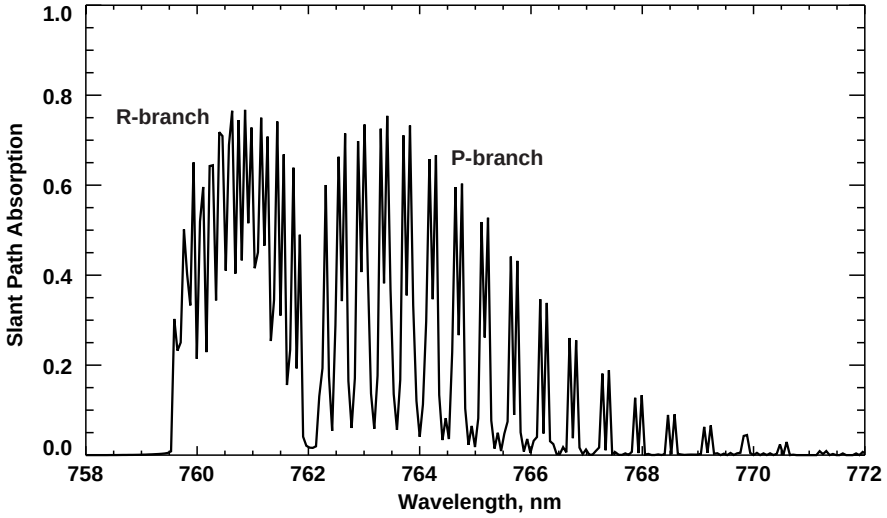

Figure 3.2.5 Detailed line structure of the oxygen A-band absorption spectrum for a slant path at 20 km (displayed at a spectral resolution of approximately 0.02 nm).

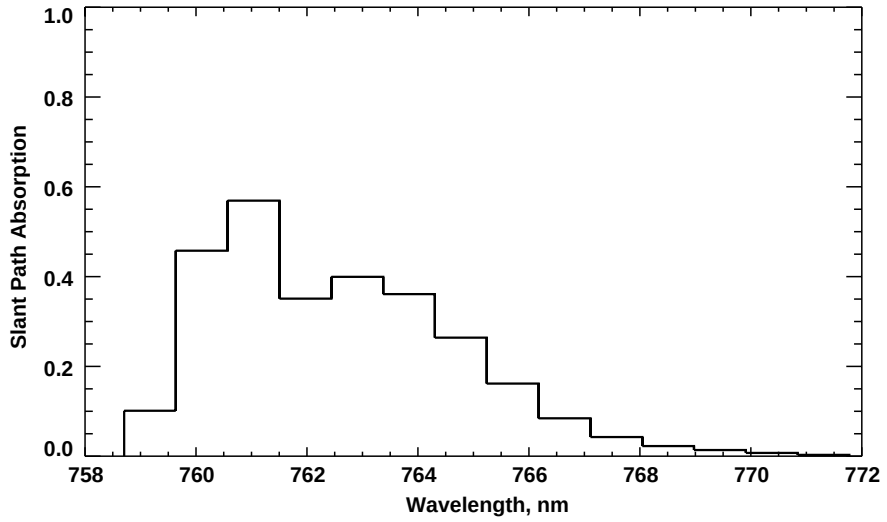

Figure 3.2.6 Structure of the oxygen A-band absorption spectrum for a slant path at 20 km (displayed at the SAGE III spectral resolution of approximately 1.4 nm).

In the global fit approach, a scalar merit function, χ^2, is defined as

$$\chi^2 = \sum_{i=1}^{M} \left[\frac{A_i^m - A_i^c(\mathbf{a})}{\sigma_i} \right]^2 \tag{3.2.16}$$

where A_i^m is the measured A-band slant path absorptivity for a given channel and tangent altitude with associated measurement uncertainty σ_i; A_i^c is the corresponding modeled absorptivity calculated using the forward model; **a** is the vector of temperature and pressure values from a trial solution set of profiles; and M is the total number of measurements from all channels and tangent heights (nominally *M*=1260). The merit function is simply the sum of the squares of the differences between the measured and modeled absorptivities weighted by the corresponding measurement uncertainty. Profiles of best-fit temperature and pressure values are determined by the minimization of this merit function. However, due to the non-linearity of the problem, the minimization must proceed iteratively.

An updating equation can be defined in terms of the gradient of χ^2 with respect to the temperature and pressure parameters as follows

$$\nabla \chi^2_{\min} = \nabla \chi^2_{curr} + \frac{\partial \nabla \chi^2}{\partial a_k} \Delta a_k, \tag{3.2.17}$$

where a_k are the trial solution temperature and pressure values at each tangent altitude and Δa_k are the desired adjustments to the trial solution that will minimize χ^2. We make the basic assumption that $\nabla \chi^2$ vanishes when χ^2 is a minimum ($\nabla \chi^2_{\min} = 0$), so the updating equation can be reduced to

$$-\nabla \chi^2_{curr} = \frac{\partial \nabla \chi^2}{\partial a_k} \Delta a_k. \tag{3.2.18}$$

Based on the expression for χ^2 in Equation (3.2.16), $\nabla \chi^2$ has the components

$$\nabla \chi^2 = \frac{\partial \chi^2}{\partial a_j} = -2 \sum_{i=1}^{M} \frac{\left[A_i^m - A_i^c(\mathbf{a}) \right]}{\sigma_i^2} \frac{\partial A_i^c(\mathbf{a})}{\partial a_j}. \tag{3.2.19}$$

Taking an additional derivative with respect to the temperature and pressure parameters, a_k, yields

$$\frac{\partial \nabla \chi^2}{\partial a_k} = 2\sum_{i=1}^{M} \frac{1}{\sigma_i^2} \left\{ \frac{\partial A_i^c(\mathbf{a})}{\partial a_j} \frac{\partial A_i^c(\mathbf{a})}{\partial a_k} - \left[A_i^m - A_i^c(\mathbf{a}) \right] \frac{\partial^2 A_i^c(\mathbf{a})}{\partial a_j \partial a_k} \right\}. \qquad (3.2.20)$$

By convention, the factors of 2 in Equations (3.2.19) and (3.2.20)are typically eliminated by defining

$$\beta_j \equiv -\tfrac{1}{2} \nabla \chi^2 = \sum_{i=1}^{M} \frac{\left[A_i^m - A_i^c(\mathbf{a}) \right]}{\sigma_i^2} \frac{\partial A_i^c(\mathbf{a})}{\partial a_j} \qquad (3.2.21)$$

and

$$\alpha_{jk} \equiv \tfrac{1}{2} \frac{\partial \nabla \chi^2}{\partial a_k} = \sum_{i=1}^{M} \frac{1}{\sigma_i^2} \left\{ \frac{\partial A_i^c(\mathbf{a})}{\partial a_j} \frac{\partial A_i^c(\mathbf{a})}{\partial a_k} - \left[A_i^m - A_i^c(\mathbf{a}) \right] \frac{\partial^2 A_i^c(\mathbf{a})}{\partial a_j \partial a_k} \right\}. \qquad (3.2.22)$$

With the definitions of α_{jk} and β_j given above, the updating expression, Equation (3.2.18), can now be rewritten as the set of linear equations with N unknowns

$$\beta_j = \sum_{k=1}^{N} \alpha_{jk} \Delta a_k . \qquad (3.2.23)$$

In matrix-vector notation, this set of equations can be written as

$$\mathbf{b} = \mathbf{K} \Delta \mathbf{a} , \qquad (3.2.24)$$

where **b** is a vector with components β_j, **K** is the kernel matrix with elements α_{jk}, and Δ**a** is the vector whose components are the unknown temperature and pressure adjustments, Δa_k. The general solution to this set of equations is

$$\Delta \mathbf{a} = \mathbf{a}^{n+1} - \mathbf{a}^n = \mathbf{K}^{-1} \mathbf{b} \qquad (3.2.25)$$

where $\mathbf{K}^{-1}$ indicates the matrix inverse of **K** and the superscripts *n* and *n+1* indicate iterated solutions for the temperature and pressure profile vector (after each iteration, the temperature and pressure adjustments, Δ**a,** are added to a trial solution profile of temperature and pressure, $\mathbf{a}^n$, to produce a new trial solution profile, $\mathbf{a}^{n+1}$).

A modified Levenberg-Marquardt non-linear least squares procedure [Levenberg, 1944; Marquardt, 1963] will be used to iteratively solve this linear set of equations. The Levenberg-Marquardt method is a well-known minimization procedure that has become a standard of non-linear least-squares routines [Press *et al*., 1992] and its application to the retrieval of atmospheric parameters from limb measurements has been demonstrated by Carlotti [1988] and Wang *et al*. [1992]. A distinct advantage of this approach is its ability to smoothly alternate between two different minimization methods as conditions warrant. Initially, when far from the minimum, the Levenberg-Marquardt method takes large steps

using the steepest descent method to minimize χ^2 and then gradually changes to the more refined inverse-Hessian method as the minimum in χ^2 is approached. Adopting the Levenberg-Marquardt scheme, the temperature and pressure adjustments are determined by solving a modified linear system defined by

$$\Delta \mathbf{a} = \left(\mathbf{K} + \lambda \mathbf{I}\right)^{-1} \mathbf{b}. \tag{3.2.26}$$

In this expression, **I** is the identity matrix and λ is the Levenberg-Marquardt constant that controls the minimization path taken. For very large values of λ, the formulation reduces to the steepest descent method; for very small values of λ it reduces to the inverse-Hessian method. Press *et al.* [1992] provides insight into the initial choice of λ and how to reduce it as the minimum is approached. In our implementation, λ is initially set to a value of 0.1 and is reduced by a factor of 10 after each successful iteration.

One of the strengths of the Levenberg-Marquardt method is the ability to directly estimate the errors in the retrieved parameters. Once the retrieval has converged, the covariance matrix of the standard errors in the retrieved temperature and pressure parameters is determined by setting λ=0 and computing

$$\mathbf{C} = \mathbf{K}^{-1}. \tag{3.2.27}$$

The diagonal elements of **C** are the variances (squared uncertainties) in the retrieved temperature and pressure values, while the off-diagonal elements are the covariances between the retrieved parameters. The covariance provides information on inter-level correlation between errors in the retrieved temperature and pressure values. It is important to note that the information contained in the covariance matrix is meaningful only if the estimates of uncertainty in the measured absorptivities, σ_i, are realistic assessments for that particular retrieval scenario. These uncertainties include both random measurement noise and the error in removing the interfering aerosol and ozone components from the oxygen A-band signal.

A suitable convergence test is required to terminate the iteration process. Press *et al.* [1992] recommends stopping the Levenberg-Marquardt process when the decrease in χ^2 between successive iterations becomes negligible. In simulated retrievals, little improvement is found in the solution when χ^2 decreases by less than 1% and therefore the retrievals are terminated when this criterion is met.

The retrieval algorithm requires first-guess temperature and pressure profiles to begin the iteration process. Operationally, the first-guess profiles will be derived from the NCEP operational global analyses. Above 40 km, these profiles will be supplemented with data derived from the GRAM-95 climatological model [Justus et al., 1995]. A schematic overview of the complete retrieval process is shown in Figure 3.2.7.

Forward Model Calculations

The ability to retrieve accurate temperature and pressure profiles from the oxygen A-band measurements depends not only on the accuracy of the SAGE III measurements themselves, but also on an accurate forward model as well. The most accurate approach for calculating the channel-averaged molecular oxygen absorptivities would be the so-called line-by-line method. In this procedure, the molecular oxygen cross sections are first computed in very narrow spectral intervals and then integrated over the atmospheric path to produce "monochromatic" slant path transmissivities. The transmissivities are then combined with the exoatmospheric solar radiance and instrument response function and integrated over wavenumber to produce the channel-averaged slant path absorptivities. This method, however, is far too time-consuming for operational processing.

An alternative numerical approach to calculate broadband absorptivity for inhomogeneous paths at both the speed and accuracy necessary for operational data processing is the Emissivity Growth Approximation (EGA). The EGA method was first suggested for transmittance calculations by Weinreb and Neuendorffer [1973] and later reformulated for emissivity calculations by Gordley and Russell [1981]. This technique has proven successful for operational forward model calculations in a number of limb viewing satellite experiments [Chu *et al.,* 1993; Marshall *et al.,* 1994]. A detailed description of the EGA technique and its application to the SAGE III forward model calculations of molecular oxygen slant path absorptivity can be found in Appendix B.

Simulation Studies

The retrieval algorithm together with the forward model form the basic tools necessary to simulate realistic SAGE III temperature and pressure retrievals. In lieu of actual measurements, synthesized measurements will serve as the primary means to validate the retrieval approach. To simulate realistic measurements, a component of random noise is added to the synthetic measurements generated with the forward model. The random noise is assumed to be Gaussian with a standard deviation based on the estimated signal-to-noise ratio of 3000.

Results of a simulated retrieval for an Arctic winter test case using synthetic measurements with realistic noise are shown in Figure 3.2.8. The first-guess, "true", and retrieved temperature profiles are depicted as the dotted, dashed, and solid lines in panel (a), respectively; while the actual differences between the "true" and retrieved temperature profiles are illustrated in panel (b). The first-guess, "true", and retrieved pressure profiles and differences are similarly displayed in panels (c) and (d). The effect of measurement noise is readily apparent as it produces oscillations in the retrieved products, especially above about 40 km. Below 40 km, the retrieved data reproduce the

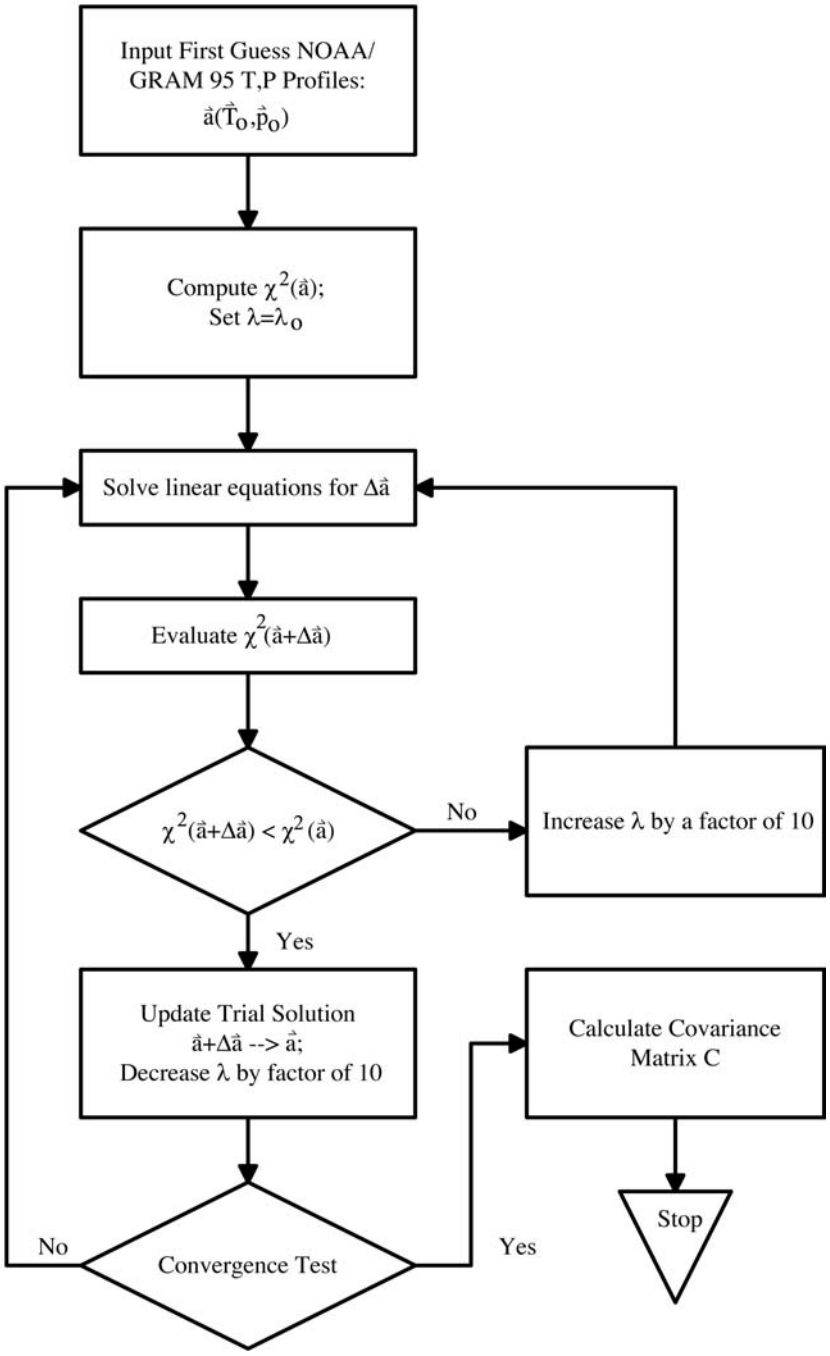

Figure 3.2.7 Flow diagram of the SAGE III temperature and pressure retrieval algorithm.

"true" atmosphere extremely well. The solid lines in the difference plots (panels b and d) represent the magnitude of the standard errors in the retrieved temperature and pressure profiles determined from the covariance matrix of the inversion. With few exceptions, these standard error values bracket the observed differences between the "true" and retrieved atmospheric states and are reasonable estimates of the expected uncertainty in retrieved parameters due to measurement noise.

The noise-induced oscillations in the retrieved temperature and pressure profiles such as those shown in Figure 3.2.8 are not representative of real atmospheric variability and therefore are undesirable. In an effort to reduce the magnitude of these oscillations, a hydrostatic constraint has been implemented. For SAGE III, temperature and pressure are retrieved simultaneously and it is difficult to directly impose a rigid hydrostatic constraint on the solution. As an alternative approach, we have formulated a hydrostatic constraint in terms of an additional set of equations that can be included in the minimization process. In this way, the retrieved atmosphere is not strictly required to satisfy the hydrostatic equation, but instead is pushed towards hydrostatic equilibrium within the expected bounds of the approximation in a more implicit sense. The results of a simulated constrained retrieval are shown in Figure 3.2.9. The hydrostatic constraint significantly reduces the magnitude of the oscillations in the retrieved temperatures and pressures above 40 km that were present in the unconstrained case (Figure 3.2.8). The differences between the "true" and retrieved temperatures are reduced by a factor of 2 or greater above 50 km using the hydrostatic constraint. The improvement in the pressure retrieval is even better with the differences now less than 1% over the entire altitude range. The standard errors from the covariance matrix (solid lines in Figure 3.2.9b and Figure 3.2.9d) are also significantly smaller, reflecting the better agreement observed between the retrieved parameters and the "true" atmosphere.

Uncertainty Estimates: Temperature and Pressure

Following the formal approach of Rodgers [1989, 1990], we performed a comprehensive characterization and error analysis of the temperature and pressure retrievals. Potential sources of error in both the forward model and the inversion algorithm were identified and the sensitivity of the retrieval algorithm to these errors was studied. Table 3.2.3 provides a comprehensive list of error sources in the temperature and pressure retrievals. The magnitude of the temperature and pressure uncertainties from the various random and systematic sources listed in Table 3.2.3 were estimated individually and then combined to produce estimates of the total random, systematic, and experimental (combined random and systematic) errors. In each case, the total error is estimated as the square root of the sum of the squares of the individual contributions.

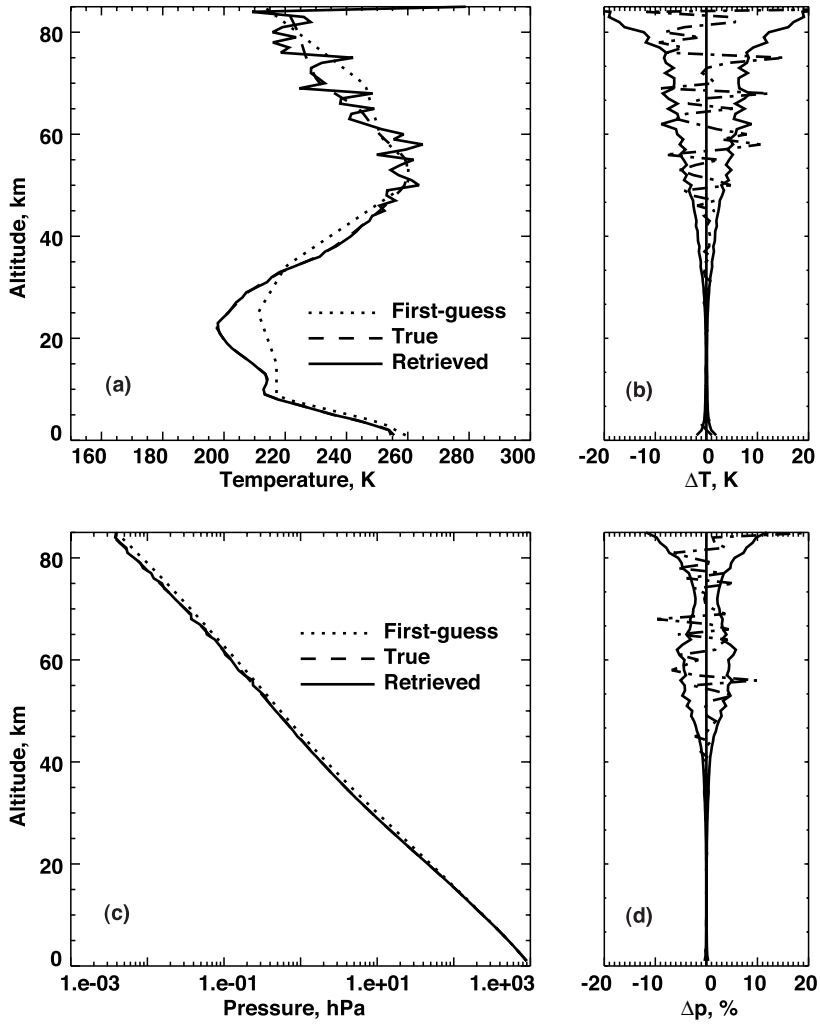

Figure 3.2.8 Simulated retrieval of Arctic winter atmosphere using synthetic measurements with realistic measurement noise (SNR=3000).

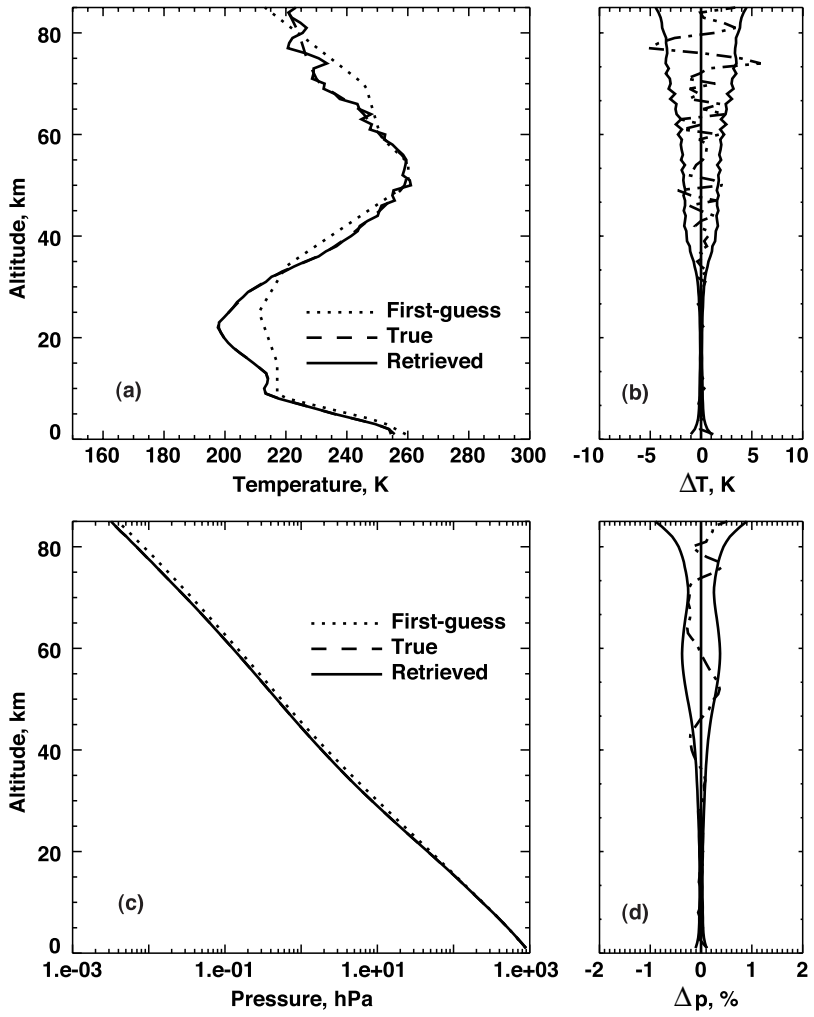

Figure 3.2.9 Simulated retrieval of Arctic winter atmosphere with the hydrostatic constraint.

Table 3.2.3. Error sources

Source	Magnitude
Random	
Measurement noise	SNR=3000
Aerosol clearing	1.0% of aerosol SPOD
Ozone clearing	0.5% of ozone SPOD
Systematic	
O_2 spectroscopy:	
-Line strengths	1.0%
-Half-widths	2.5%
-Temperature exponent	15%
-Line centers	0.015 cm^{-1}
O_3 cross sections	1.0%
EGA accuracy	<5%

The total random error in the retrieval consists of contributions due to measurement noise and errors in clearing the aerosol and ozone components from the A-band signal (dotted lines in Figure 3.2.10). The dominant source of random error in the retrieved temperatures is measurement noise. Random errors in the retrieved pressures are also dominated by measurement noise above 50 km, but ozone and aerosol clearing errors become dominant below this altitude.

The total systematic error in the retrieval (dot-dashed lines in Figure 3.2.10) consists of contributions from the oxygen and ozone spectroscopy errors and the Emissivity Growth Approximation (EGA) radiative transfer calculation errors. The dominant source of systematic error in both the retrieved temperatures and pressures below about 30 km is bias in the exponent of the temperature dependence of the Lorentz half-widths. Between about 30 and 65 km, both EGA and ozone spectroscopy uncertainties are the most important sources of systematic error. Above 65 km, bias in the oxygen line strengths becomes the dominant source of systematic error in pressure, while the systematic errors in temperature are due to a combination of line strength, line position, and EGA errors.

The total estimated experimental error in the retrieved temperature and pressure profiles due to all random and systematic sources is shown as the solid lines in Figure 3.2.10. Systematic error overwhelms random error in the pressure retrievals and dominates the total uncertainty in pressure at all altitudes. Systematic error also dominates the temperature uncertainties below about 30 km, while measurement noise becomes the dominant source of temperature error above about 40 km.

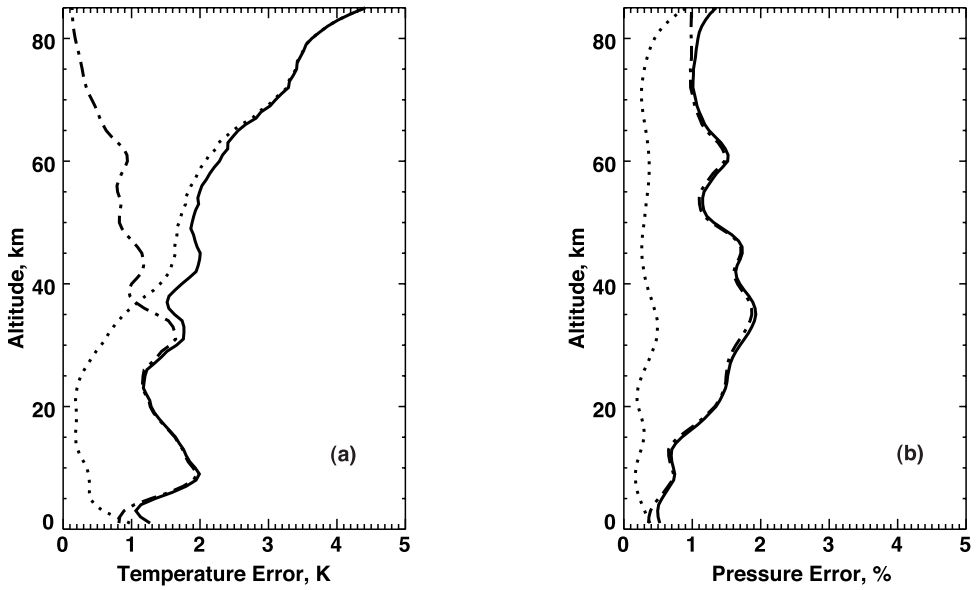

Figure 3.2.10 Total experimental error (solid lines) in the retrieved temperature and pressure profiles due to all random and systematic sources estimated by combining the root-sum-square of the total random (dotted lines) and systematic (dot-dashed lines) components.

3.2.6 Reduction of Slant Column Densities to Vertical Profiles.

The final stage of the inversion process consists of the reduction of slant path column molecular densities to vertical profiles of molecular number densities. This will follow the SAGE II processing method in which a modified Chahine method [Chahine, 1972; Twomey, 1975; Chu *et al.,* 1979 and 1989; Chu, 1985] was employed though alternative methods will be examined. With all species transformed to vertical profiles, construction of the data products listed in Table 1.6.1 is executed and the data made available for archival.

The construction of the slant column density profile for ozone is unique due to the fact that information on ozone comes from two different measurements. Slant column densities are estimated from the 290nm extinction measurements at high altitude. The slant column profiles will be combined in to a single profile covering the entire range which will then be inverted to a single ozone density profile. The combination procedure will be based on error estimates from each type of slant column estimation and appropriate quality flags will be set indicating the primary source of information at each altitude.

For species which have a significant diurnal variation across the terminator, the assumption of inhomogeneous spherical shells is incorrect. Nevertheless, the assumption will be maintained for the inversion process. In addition, the slant column density profile will be archived for those users wishing to model in detail the variations along the line of sight with heterogeneous photochemical trajectory models.

3.3 Algorithm Testing Requirements

Algorithm testing will be performed both prior to launch and during the lifetime of the instrument using the SAGE III data simulator. The data simulator models both a ray tracing-based model of the atmosphere and accounts for measured and modeled instrument performance. For instance, the instrument model includes the effects of uncertainties in the instrument wavelength-band pass, fields of view, detector response, and spacecraft telemetry. The atmospheric model can include realistic uncertainties in errors in external data sets (e.g., molecular spectroscopy and lunar albedo) and the effects of atmospheric spatial inhomogeniety. The simulator should (and has) helped us to identify software errors and below standard performance in individual retrieval components. The simulator is maintained under configuration control and is considered an adjunct component of the primary operational software.

3.4 Validation Plan

Planning for the validation of all SAGE III data products is covered in the SAGE III Validation Plan (LaRC475-00-020). Validation plans are uncertain due to the slip in SAGE III/Meteor-3M launch date and that document will be revised as launch date and funds available for validation become more certain.

3.5 Quality Control and Diagnostics

Routine processing will generate a series of quality indicators that assess the quality of the data products and the degree to which the processing of each event was completed according to expectation. The details of this process are outlined in The SAGE III Data Management System Quality Assurance Document (LaRC475-03-115).

4.0 Lunar Algorithm Description

4.1 Introduction

SAGE III provides unique capabilities to measure nocturnal species concentrations and to obtain increased geographic and temporal coverage of data by using the moon as a radiance source. Unique challenges posed by using the moon as a radiance source include the spatial and spectral non-uniformity of the lunar albedo, the variation in lunar illumination as a function of lunar phase, and the moon's relatively low brightness (one millionth the solar brightness). To reduce the lunar data, certain unique algorithm approaches which differ significantly from the solar approaches, are required.

The non-uniformity of the lunar albedo precludes the calculation of an exoatmospheric radiance value; therefore, calculation of an absolute atmospheric transmission, as is done with the sun, is not possible. To calculate the slant path column densities, the lunar inversion algorithm uses a multiple linear regression fit of the high frequency components of the measured spectral data and the high frequency components of the absorption cross sections. This technique is described in detail below.

To accomplish the lunar position registration, a technique was developed which uses a radiometric model of the moon. In the solar case, the scan plane of the instrument's field of view is assumed to pass through the radiometric center (and the geometric center) of the sun. The top and bottom edge signatures are determined, and the observation points are then placed on the target solar disk. In the lunar case, the radiometric center of the moon will not usually correspond to the geometric center; additionally, the moon's terminator may preclude using either the top or bottom edge of the moon for the position registration. The lunar altitude registration, described in detail in Appendix E, uses a radiometric model to determine the moon's brightness centroid and terminator location. A single edge signature is determined, and remaining points in the scan are placed by relative mirror position.

4.2 Lunar Differential Retrievals of Gases

Differential retrievals offer a direct computational means of separating aerosol extinction and gaseous absorption features. The following discussion focuses on the lunar occultation problem, but applies equally well to solar occultation, as will be the case for the retrievals of ozone and nitrogen dioxide. Lunar occultation retrievals of atmospheric extinction are considerably more complicated than the solar occultation measurements as a result of the spatial and spectral non-uniformity of the surface albedo of the Moon. Consequently, the accuracy of the lunar limb-darkening curves that are used to calibrate each SAGE occultation event preclude the production of absolute transmission profiles during lunar occultation. Secondarily, given the relatively low signal-to-noise ratios in lunar occultation measurements, single channel measurements are insufficient to meet the

SAGE III measurement objectives; instead measurements from many channels are combined together to reduce the random measurement error (precision) to a level consistent with the performance goals for SAGE III lunar measurements. In the absence of an accurate exoatmospheric calibration, retrievals which utilize measurements over a broad spectral range must be performed in a fashion that is insensitive to broadband continua and extinction; one such approach is a differential measurement technique on the absorption spectrum. The observed lunar radiance is

$$I = aI_0 e^{-T} e^{-\tau}, \tag{4.2.1}$$

where aI_0 is a scaled solar spectrum, and e^{-T} and $e^{-\tau}$ are broadband and narrowband (mostly atmospheric molecular absorption) features in the spectrum, respectively. The method under evaluation takes the natural logarithm of (4.2.1) to obtain

$$\ln(I / \overline{A}\, I_0) = \ln(Ae^{-T}) - \tau. \tag{4.2.2}$$

The lunar albedo has been expressed as $\overline{A}A$, where $\overline{A}$ is the mean albedo and A contains some spectral information unique to the Moon. In the case of solar occultation, $\overline{A}A$ is unity. Figure 4.2.1 depicts a scaled solar spectrum and Figure 4.2.2 depicts a mean albedo. Strictly speaking the lunar albedo will probably have some higher frequency (narrow band) components which pass through the filter. For clarity, these terms will not be included in subsequent discussion and equations, however, they will be included in the retrieval. The observed lunar spectrum (I) has been divided by a scaled solar spectrum ($\overline{A}\, I_0$). After taking the natural logarithm, terms may be separated in to broadband ($\ln(Ae^{-T})$) and narrowband, molecular (τ) components. By definition, the term, τ, contains only the high frequency components of the observed spectra.

In order to obtain the term τ, the low frequency components

$$\ln(Ae^{-T}) \tag{4.2.3}$$

must be estimated. The four filter types were developed and tested for evaluating (4.2.3) from the data. Each type was used to obtain the differential spectrum by subtracting the "low pass filter" result from the log of the ratio spectra. The filters are:
A fast Fourier transform filter with an adjusted cutoff frequency to determine the low frequency components, a finite impulse response filter to determine the low frequency components, a least-squared fit to a second or third order polynomial to approximate the low- frequency components, and a singular value decomposition (SVD) fit to a second or third order polynomial to approximate the low frequency components.

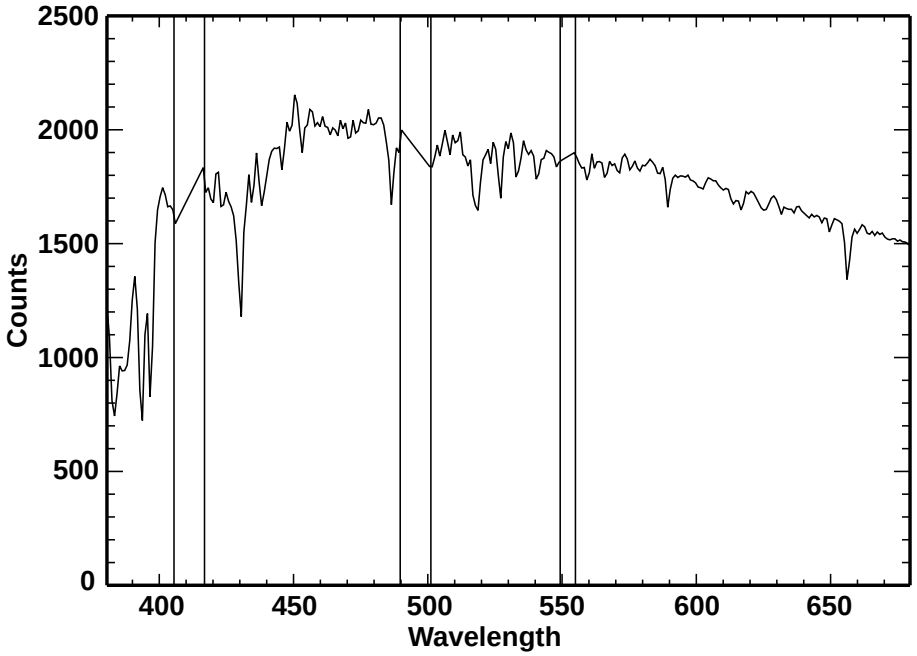

Figure 4.2.1 Scaled solar spectrum with channel gaps.

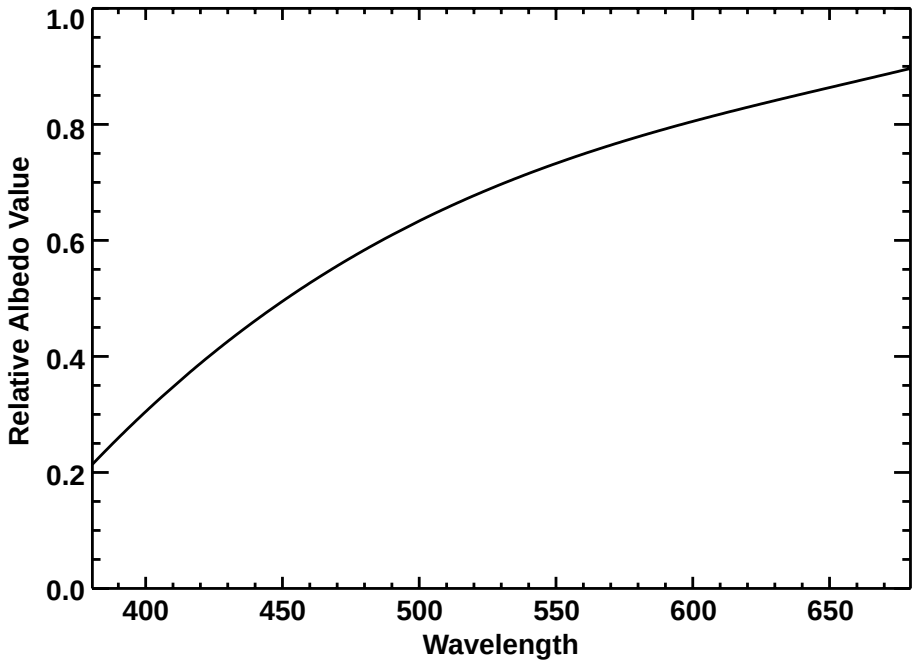

Figure 4.2.2 Relative lunar albedo curve.

The following techniques were tested in conjunction with each of the above filter types to improve the overall filter performance:

1. The ratio data were filtered over wavelength intervals of various widths, with emphasis on the channel gaps depicted above, and using different combinations of polynomial order.
2. To smooth the data, the logarithm of the ratio data was taken, fitted with a low frequency wave form, and the exponential function of the fitted curve was subtracted from the original ratio data.
3. The ratio data were fitted with weighted curves to obtain an improved fit.

The best results for filtering the ratio data and removing the low frequency components were obtained by making a composite differential spectrum, by a combination of the above filter types and techniques, applied over different segments of the lunar pixel wavelengths. Figure 4.2.3 shows a composite differential spectrum at 25 km. Additionally, using iterations and species clearing, (described in section below) in conjunction with filtering over a wider spectral range yielded a slight increase in the final retrieval accuracy. Ground-based measurements of the solar and lunar spectrum will be made using an engineering model of the SAGE III spectrometer (VU). These data will be used to refine the filtering scheme as well as to identify narrow band features in the lunar spectral albedo.

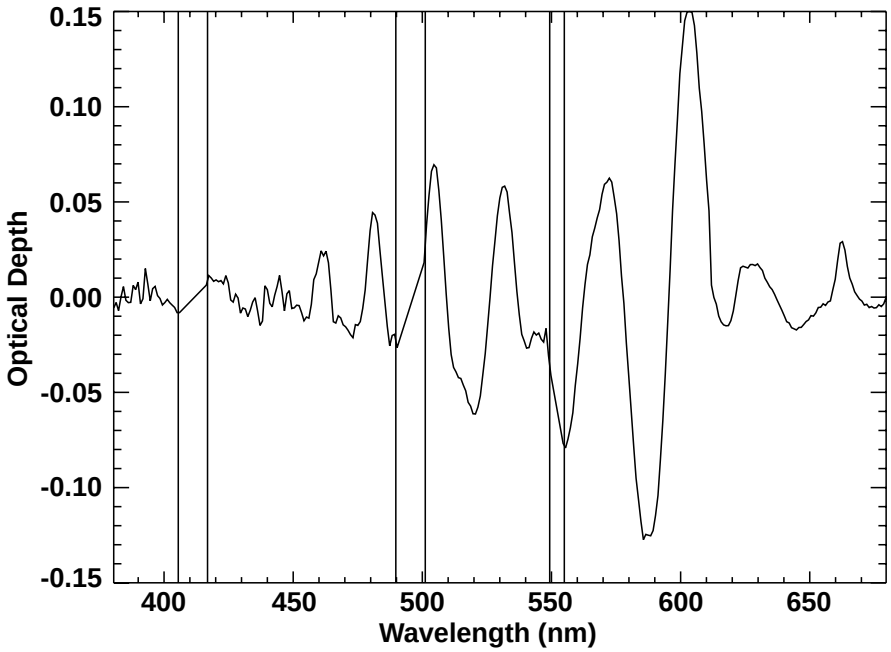

Figure 4.2.3 Composite differential spectrum after filtering by segments.

The differential spectrum is ideally suited for multiple linear regression analysis, as is indicated in the following sections. To optimize the number of channels available for analysis, the majority (~ 300) of the lunar occultation channels are contiguous between 380 and 680 nm, from which ozone, nitrogen dioxide, nitrogen trioxide, and chlorine dioxide will be measured. This differential spectrum will also contain any high frequency information contained in the lunar albedo and must be allowed for in the regression analysis. A channel selection for O_2 and H_2O will be similar to that used in solar occultation. Aerosol and cloud are not intended as standard products from the lunar occultation measurements.

MLR Equations

The formulation of the inverse problem after filtering the data follows the same methodology used in the aerosol/ozone retrieval problem. Here Equation (3.2.5) is expressed as

$$\tau(\lambda_i) = n_{O_3}\sigma_i(\lambda_i, O_3) + n_{NO_2}\sigma_i(\lambda_i, NO_2) + n_{H_2O}\sigma_i(\lambda_i, H_2O) + n_{NO_3}\sigma(\lambda_i, NO_3) + n_{OClO}\sigma(\lambda_i, OClO) \tag{4.2.4}$$

or in a matrix form

$$\begin{bmatrix} \tau_{380} \\ \tau_{381} \\ . \\ . \\ . \\ \tau_{680} \end{bmatrix} = \begin{bmatrix} \sigma_{380}(O_3) & \sigma_{380}(NO_2) & \sigma_{380}(H_2O) & \sigma_{380}(NO_3) & \sigma_{380}(OClO) \\ \sigma_{381}(O_3) & \sigma_{381}(NO_2) & \sigma_{381}(H_2O) & \sigma_{381}(NO_3) & \sigma_{381}(OClO) \\ \cdots & \cdots & \cdots & \cdots & \cdots \\ \cdots & \cdots & \cdots & \cdots & \cdots \\ \cdots & \cdots & \cdots & \cdots & \cdots \\ \sigma_{680}(O_3) & \sigma_{680}(NO_2) & \sigma_{680}(H_2O) & \sigma_{680}(NO_3) & \sigma_{680}(OClO) \end{bmatrix} \begin{bmatrix} n_{O_3} \\ n_{NO_2} \\ n_{H_2O} \\ n_{NO_3} \\ n_{OlCO} \end{bmatrix} \tag{4.2.5}$$

The solution of this problem will follow the same processing method described in Section 3.2.3.

Simulated lunar occultation observations generated by a complex forward simulation model were used to begin development of differential MLR procedures. The simulation incorporated a solar spectrum ranging from 380 nm to 680 nm, reflected by a modeled lunar disk with variable albedo, ray tracing through the atmosphere, and the effects of Rayleigh scattering and absorption by molecular gases and aerosols. Chemical species absorption was simulated by using typical night time concentrations for O_3, NO_2, NO_3, and OClO. The key steps in the MLR retrieval process under development are as follows:

1. Approximate I_0 from the scaled solar spectrum and the average albedo curve (Figure 4.2.1 and 4.2.2).
2. Calculate -ln(I/I_0).
3. Filter -ln(I/I_0) results by procedures described in previous section.
4. Filter the absorption cross section by the same procedure.
5. Perform MLR per Equation (4.2.4) to obtain column densities.

After the initial column density computation, the absorption contribution by a species may be removed by multiplying the column density value by the absorption cross section and subtracting from the ratio data. This technique is employed in the inversion algorithm prior to iterating steps 2 through 5 above using a different set of filters. Figure 4.2.4 shows the results of O_3 column density calculation before and after iteration. Figure 4.2.5 show the simulated O_3, NO_3 and OClO errors for a lunar event.

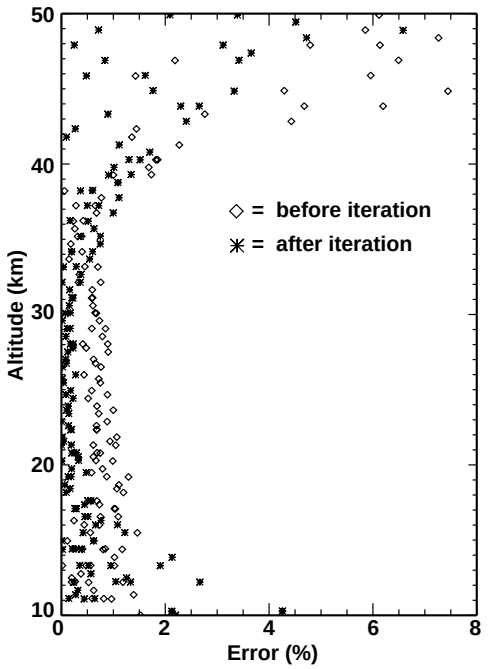

Figure 4.2.4 O_3 profile absolute error before and after iteration.

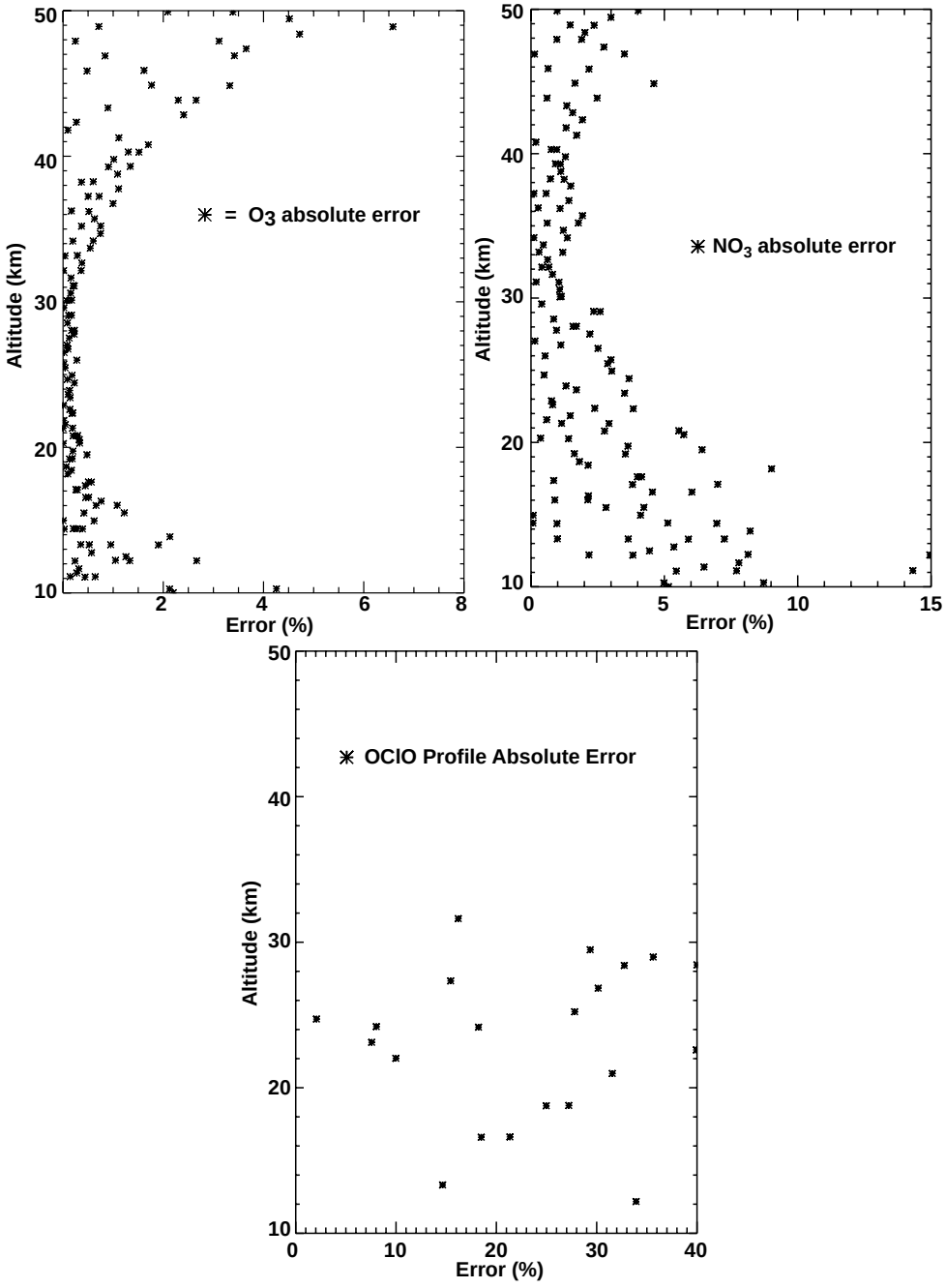

Figure 4.2.5 Simulation of a multi-channel O_3, NO_3 and OClO measurement from lunar occultation measurements (forward simulation model).

5.0 References

Bevington, P. R., *Data Reduction and Error Analysis For the Physical Science*, McGraw-Hill, N. Y., 1969.

Carlotti, M., Global-fit approach to the analysis of limb-scanning atmospheric measurements, *Appl. Opt.*, 27, 3250-3254, 1988.

Chahine, M. T., A general relaxation method for inverse solution of the full radiative transfer equation, *J. Atmos. Sci*., 29, 741-747, 1972.

Chu, W., and M. P. McCormick, Inversion of stratospheric aerosol and gaseous constituents from spacecraft solar extinction data in the 0.38-1.0 micron wavelength region, *Appl. Opt*., 18, 1404-1414, 1979.

Chu, W. Calculation of atmospheric refraction for space craft remote sensing applications, *Appl. Opt*., 22, 721-726, 1983.

Chu, W. P., Convergence of Chahine's nonlinear relaxation inversion method used for limb viewing remote sensing, *Appl. Opt*., 24, 445-447, 1985.

Chu, W. P., M. P. McCormick, J. Lenoble, C. Brogniez, and P. Pruvost, SAGE II inversion algorithm, *J. Geophys. Res*., 94, 8339-8351, 1989.

Chu, W. P., E. W. Chiou, J. C. Larsen, L. W. Thomason, D. Rind, J. J. Buglia, S. Oltmans, M. P. McCormick, and L. M. McMaster, Algorithms and sensitivity analyses for Stratospheric Aerosol and Gas Experiment II water vapor retrieval, *J. Geophys. Res.,* 98, 4857-4866, 1993.

Gordley, L. L., and J. M. Russell, A fast and accurate radiance algorithm for applications to inversion of limb measurements*, in Remote Sensing of Atmospheres and Oceans*, edited by A. Deepak, p. 591, Academic Press, San Diego, Calif., 1980.

IPCC, 1996: *Climate Change 1995: The IPCC Second Assessment Report,* Cambridge University Press, in press, 1996. Advance copy of Summary for Policymakers: The Science of Climate Change, IPCC Working Group I (1995) available on http://www.unep.ch/ipcc/sumwg1.html.

Justus, C. G., W. R. Jeffries, S. P. Yung, and D. L. Johnson, The NASA/MSFC Global Reference Atmosphere Model-1995 Version, NASA TM 4715, 1995.

Levenberg, K., A method for the solution of certain nonlinear problems in least squares, *Quart. Appl. Math*., 2, 164-169, 1944.

Marshall, M. P., and A. C. Neuendorffer, Method to apply homogeneous-path transmittance models to inhomogeneous atmospheres, *J. Atmos. Sci.,* 30, 662-666, 1973.

Marquardt, D.W., An algorithm for least-squares estimation of nonlinear parameters, *J. Soc. Indust. Appl. Math.,* 11, 431-441, 1963.

Mauldin, L. E., Stratospheric Aerosol and Gas Experiment II instrument: a functional description, *Opt. Eng*., 24, 2, 307-312, 1985.

Mauldin, L. E., M. P. McCormick, J. M. Zawodny, L. R. McMaster, W. P. Chu, J. C. Gustafson, and G. L. Maddrea, The Stratospheric Aerosol and Gas Experiment III instrument proposed for EOS: a conceptual design, *Int. Congress on Opt. Sci. and Eng*. - Paris, France, 1989.

McCormick, M. P., P. Hamill, T. J. Pepin, W. P. Chu, T. J. Swissler, and L. R. McMaster, Satellite studies of the stratospheric aerosol, *Bull. of the Amer. Met. Soc*., 60, 9, 1979.

McCormick, M. P., W. P. Chu, G. W. Grams, P. Hamill, B. M. Herman, L. R. McMaster, T. J. Pepin, P. B. Russell, H. M. Steele, and T. J. Swissler, High-latitude stratospheric aerosol measured by SAM II satellite system in 1978-1979, *Science*, 214, 328-331, October, 1981.

McCormick, M. P., SAGE II: an overview, *Adv. Space Res*., 7, 3, (3)219-(3)226, 1987.

McCormick *et al*., Stratospheric Aerosol and Gas Experiment III (SAGE III) Aerosol and trace gas measurements from Earth Observing System (EOS), SPIE Paper No. 1491-16, *SPIE Symposium on Aerospace Sensing*, Orlando, Florida, 1991.

McCormick, M. P., J. M. Zawodny, W. P. Chu, J. W. Baer, J. Guy, and A. Ray, Stratospheric Aerosol and Gas Experiment III (SAGE III), *SPIE International Symposium for Optical Engineering* - Orlando, FL, 1993.

Pepin, T. J. and M. P. McCormick, Stratospheric Aerosol Measurement Experiment MA-007, NASA TM X-58173, February, 1976

Press, W. H., S. A. Teukolsky, W. T. Vetterling, and B. P. Flannery, *Numerical Recipes in FORTRAN: The Art of Scientific Computing*, Cambridge University Press, New York, 1992.

Rodgers, C. D., A general error analysis for profile retrieval, *RSRM '87 Advances in Remote Sensing Retrieval Methods*, edited by A. Deepak, H.E. Fleming, and J.S. Theon, pp.285-297, A. Deepak Publishing, Hampton, Va., 1989.

Rodgers, C. D., Characterization and error analysis of profiles retrieved from remote sounding measurements, *J. Geophys. Res.,* 95, 5587-5595, 1990.

Russell, P. B., T. J. Swissler, M. P. McCormick, W. P. Chu, J. M. Livingston, and T. J. Pepin, Satellite and correlative measurements of the stratospheric aerosol, I. An optical model for data conversion, *J. Atmos. Sci*., 38, 1279-1294, 1981.

Solomon, S., R. W. Portmann, R. R. Garcia, L. W. Thomason, L. R. Poole, and M. P. McCormick, The role of aerosol variations in anthropogenic ozone depletions at northern midlatitudes, *J. Geophys. Res*., 101, 6713-6727, 1996.

Stolarski, R. S., and H. L. Wesoky, The atmospheric effects of stratospheric aircraft: A third program report, NASA Reference Publication 1313, 1993.

Twomey, S., Comparison of constrained linear inversion and an iterative nonlinear algorithm applied to the indirect estimation of particle size distributions, *J. Comput. Phys*., 18, 188-198, 1975.

Wang, P.-H., M. P. McCormick, W. P. Chu, J. Lenoble, R. M. Nagatani, M. L. Chanin, R. A. Barnes, F. Schmidlin, and M. Rowland, SAGE II stratospheric density and temperature retrieval experiment, *J. Geophys. Res*., 97, 843-863, 1992.

Marshall, B. T., L. L. Gordley, and D. A. Chu, BANDPAK: Algorithms for modeling broadban transmission and radiance, *J. Quant. Spectrosc. Radiat. Trans.,* 52, 581-599, 1994.

Appendix A. SAGE III Instrument Description

The design of the SAGE III sensor relies heavily upon the flight proven designs used in the SAM II and SAGE I/II instruments. Specifically, the separate sensor and electronics modules concept from SAGE II is utilized, as are the grommet isolation and contamination door designs. Additionally, the SAGE II pointing system and scan mirror designs are reused, with certain necessary modifications (primarily an attenuator filter) to permit solar and lunar observations with the same detector assembly.

The SAGE III sensor assembly, illustrated in Figure A.1, consists of a sun-tracker, telescope, and grating spectrometer with a CCD detector array; the mass is estimated at 35 kg., a volume of 6000 cm^3, with an average power of 60 W and a peak power of 75 W. The two-axis passive sun-tracker, with a scan mirror that scans the instrumental field of view across the solar disk, obtains multiple samples at each altitude, improving the measurement precision. Sunspots are readily detected by scanning, rather than staring at the Sun. A pictorial representation of the scanning pattern as a function of tangent altitude and the corresponding detector output (single wavelength) is illustrated in Figure A.2. The two solid lines denote the position of the top and bottom of the solar disk during a sunrise event as viewed from the spacecraft. The gradual expansion of the vertical sun shape is due to atmospheric refraction. The ordinate denotes the tangent altitude, while the abscissa denotes the event time. During an occultation event, the instrument scans the solar disk as indicated by the dashed line in the figure.

The telescope and spectrometer are illustrated in Figure A.3 and constitute new designs optimized to meet the requirements of lunar occultation measurements. The telescope is a f/4 Dall-Kirkham configured design chosen for its ease of alignment; the speed represents a tradeoff between optimum performance and spectral imaging. The spectrometer is a new design, utilizing a holographic, aberration reduced, grating to provide stigmatic imaging at 440 and 868 nm with 1 nm resolution below 450 nm and 2 nm resolution between 740 and 960 nm. The grating is formed on a spherical substrate with a radius of 152 mm and is imaged through a field flattener and order-sorting filters onto the CCD detector. The grating is utilized in the first positive order with diffraction angles between 8.3 and 17.0 degrees; a ruling of 199 lines per millimeter yields a dispersion of 0.94 to 1.88 nm per pixel in the focal plane (depending on wavelength). Evaluation gratings have been tested and demonstrate near-theoretical first-order efficiencies with very low scattered light properties. The spectrometer has been ray-traced and a Monte Carlo simulation of optical tolerances has been performed which indicates that at the wavelengths of best spectral focus, a FWHM bandpass of less than 1.2 nm per pixel should be achievable.

The detector assembly consists of two elements, a Tektronix 809x10 pixel backside-illuminated, thinned CCD array for the 280 - 1040 nm spectral region and a InGaAs infrared photodiode (1550 ± 15 nm) that are spatially co-registered. The 809 elements of the array provide the spectral information, the 10 pixels aligned along the horizontal direction are summed together and can be considered a single long pixel. Practical

considerations favor pixel subdivision: large pixels can have a low charge transfer efficiency which can be avoided through subdivision, and secondly reducing the horizontal instantaneous field of view (IFOV) can improve the probability of cloud-free measurements. Consequently, in the solar occultation mode, 3 pixels (0.5x1.5 arcminute IFOV) are used to improve the frequency of penetration of the measurements into the troposphere. In contrast, for the lunar occultation measurements, all 10 pixels are used to collect more light.

In the solar occultation mode, the optical throughput of the instrument (grating efficiency and CCD quantum efficiency) combined with the spectral variation in the solar spectrum produce a wide variation in the rate of charge accumulation in the CCD pixels as a function of wavelength. Optimum performance (signal-to-noise ratio and dynamic range) of the detector is achieved when pixels are operated at or near full well. To obtain full well across the spectral region, a spectral flattening filter was considered to selectively attenuate the spectrum near the middle of the spectral band pass, but was determined to be too difficult to design. Instead, the array has been divided into eight segments that have individually controlled integration times to control the filling of the wells. Each segment is operated at or near full well, and the transitions between segments are chosen to avoid potential science channels. This solution optimizes performance and eliminates an item of significant risk and cost.

The lunar occultation measurements are significantly more complicated than the solar measurements; depending upon phase, the Moon is between one million and ten million times less luminous than the Sun, and the lunar albedo is non-uniform making determination of atmospheric transmission non-trivial. The instrument is designed to compensate for this large change in illumination in part by removing the solar attenuator (a neutral density filter with an attenuation of 100) from the optical path. In addition, the integration time is increased from 0.09-2.2 milliseconds to 62 milliseconds (with a resulting increase in signal of 28 to 500), and the instrumental field of view is increased from 3 pixels to 10 pixels (producing an increase of 3.3 in signal level). The resulting gain increase of 165,000 should permit lunar measurements with a signal-to-noise ratio of 150-300, only a factor of 10-20 times poorer than the solar measurements which implies that the altitude range for the species retrievals will be somewhat reduced in the lunar occultation mode.

The detector package has been modeled and electrical, optical, thermal, and radiation-shielding testing of prototype detectors has been performed. The detector assembly is surrounded by an aluminum radiation shield (nominally 1-inch thick) and is illustrated in Figure A.4. The housing is comprised of a base plate, a lead frame assembly, and an optical field flattener. The lead frame assembly is an insulating rectangle through which the electrical connections to the detector and a thermoelectric cooler (TEC) pass. The field flattener is a plano-concave sapphire window. The purpose of the field flattener, in addition to providing a window to the sealed CCD package, is to further increase the radius of curvature of the focal field and coincide better with the planar CCD array.

Mounted to the backside of the field flattener are three order-sorting filters that provide the out-of-band rejection of light diffracted towards the focal plane assembly from other grating orders. The CCD is mounted to a TEC that is, in turn, mounted to the base plate heat sink. The CCD is designed with built-in thermistors that are part of an active temperature control system to meet the stability and end-of-life dark current requirements. The detector assembly has been included in the stray light analysis of the spectrometer, which showed that a significant reduction in the amount of scattered light could be achieved by rotating the CCD about its long axis by 11 degrees and eliminating internal reflections within the detector assembly. Also within the detector assembly is the InGaAs photodiode for the 1540 nm channel. This channel lies in the zero-order beam and has its band pass determined by a filter in much the same manner as was done with two of the channels in SAGE II. This detector is within the assembly because of the close proximity of the zero-order light rays to the end of the CCD array. Prototype detectors have been manufactured and tested for spectral quantum efficiency, dark current versus temperature, full-well capacity, charge transfer efficiency, and linearity. Radiation testing with monoenergetic proton beams of differing total doses have assessed the performance in a radiation environment, and led to models of energetic particle transport and secondary particle production, and an assessment of the shielding requirements for the CCD. In addition, models were developed to describe the observed temperature dependent gain of the field effect transistor preamplifiers on the CCD.

The spectrometer with the CCD array of detectors provides continuous wavelength coverage between 280 and 1040 nm and will permit the measurement of multiple absorption features of each gaseous species and multi-wavelength measurements of broadband extinction by aerosols. In the present configuration, 12 solar channels (≤80 sub-channels) will be routinely utilized in the solar occultation measurements and 3 channels (340 sub-channels) in the lunar occultation measurements, greatly decreasing the random error in the measurements (precision), and allowing for more accurate modeling of the multi-wavelength aerosol extinction. Included within the instrument band pass is the O_2 A-band (around 760 nm) which will permit the retrieval of density and temperature with which the viewing geometry (as a pressure level) can be inferred. This improvement over SAGE II, which relied upon the NOAA gridded analyses, should improve the accuracy of the SAGE III profiles and simplify the comparison with other measurements. Additionally, the linear array of detectors will permit on-orbit wavelength and intensity calibration from observations of the exoatmospheric solar Fraunhofer spectrum. The continuous spectral calibration, combined with the self-calibrating nature of the occultation technique (ratioing the signal transmitted through the atmosphere to the exoatmospheric reference signal for each measurement) makes SAGE III ideal for long-term monitoring of trends in ozone and other gas species, which is a central objective of the EOS program.

The expanded spectral coverage of the SAGE III instrument permits the observation of O_3 in the mesosphere between 65 and 85 km by utilizing the UV absorption in the short wavelength region between 385 and 290 nm and, combined with a fixed channel InGaAs detector at 1550 nm, should greatly enhance the characterization of multi-wavelength aerosol and clouds and extend this capability to lower altitudes in the troposphere. The

CCD array will provide approximately 2-nm resolution in the spectral region between 920 and 960 nm. In combination with an increase in digitization from 12 bit precision to 16 bit precision, this should allow for greater discrimination of water vapor from aerosol (both volcanic and thin cloud), and better retrieval of the higher water vapor values at lower altitudes in the troposphere than was possible with SAGE II. Table A.1 details the measurement capability of SAGE III for single profile retrievals. The notable difference, as discussed above, is the determination of pressure and temperature from oxygen A-band and the improved precision from the inclusion of additional channels.

With a 16-bit A/D converter, the SAGE III spectrometer will allow for variable integration time and on-orbit gain programming necessary for lunar observations. This potentially doubles the number of measurements per orbit, but requires a detector and signal chain that can accommodate the reduced flux observed during lunar occultations. In lunar occultation SAGE III will monitor O_3, NO_2, pressure, and H_2O, as well as OClO and NO_3.

Table A.1: SAGE III measurement capability (single profile)

Channel	Wavelength (nm)	Products	Solar Altitude	Error (%)	Lunar Altitude (km)	Error (%)
S1	290	O_3	50-85	10	----	----
S2	385	Aerosol	15-40	10	----	----
L1	380-420	OCIO	----	----	15-25	25
S3/L1	433-450	NO_2, Aerosol	10-50, 10-40	15 ----	20-50	10
L1	470-490	O_3	----	----	16-35	10
S4	521	Aerosol, Cloud	6-40	10 ----	----	----
S5	560-616	O_3	6-60	5	----	----
L1	640-680	NO_3	----	----	20-55	10
S6	670	Aerosol	3-40	5	----	----
S7	758	Aerosol	3-40	5	----	----
S8/L2	759-771	Pressure, Temperature	0-85, 0-85	2 2K	---- ----	---- ----
S9	869	Aerosol	0-40	5	----	----
S10/L3	933-960	H_2O,	0-50,	15	----	----
S11	1020	Aerosol, Cloud	0-40	5	----	----
S12	1540	Aerosol, Cloud	0-40	5	----	----

a. Error is estimated precision.
b. Lowest altitude is determined by cloud top height.

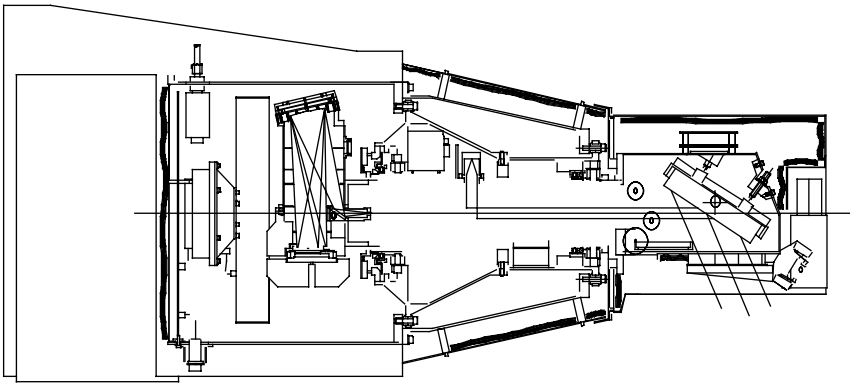

Figure A.1. The SAGE III sensor assembly.

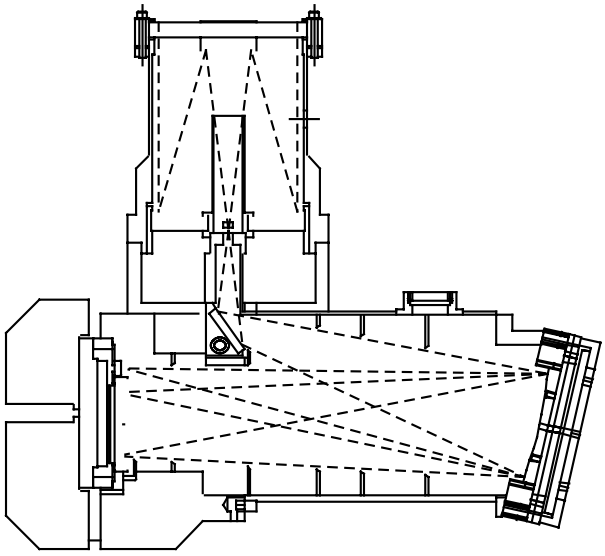

Figure A.2. Optical configuration and ray paths for the SAGE III telescope and spectrometer.

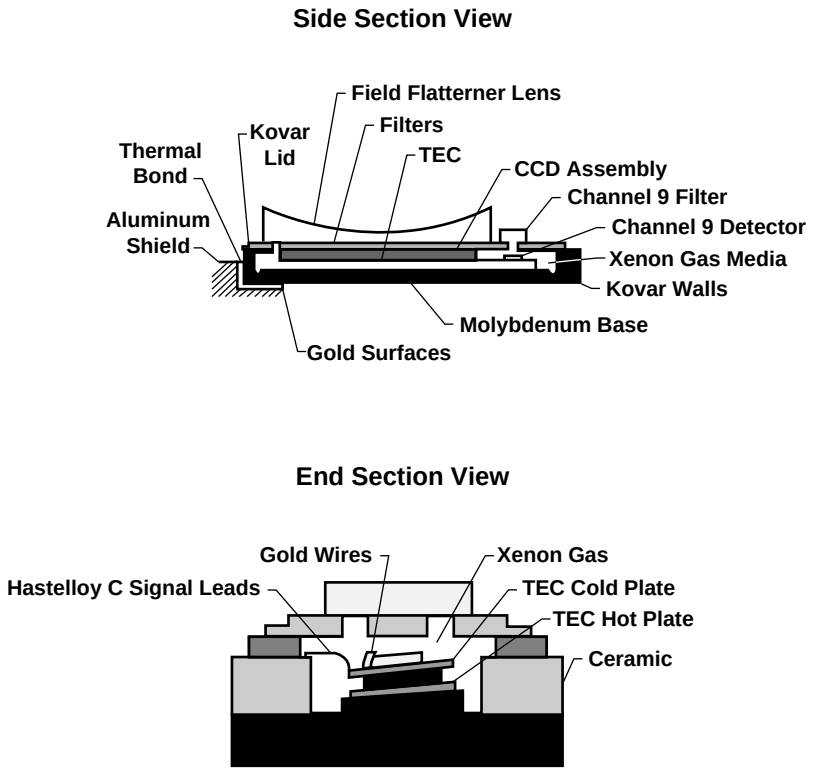

Figure A.3. SAGE III detector package.

Appendix B. Implementation of Emissivity Growth Approximation (EGA)

The retrieval of channels which involve spectroscopic calculation of individual spectral lines contribution employs EGA the technique of Gordley and Russell [1980]. This technique involves the precalculation of a grid of transmissions as a function of temperature, pressure and mass path. From the observed atmospheric absorption and an assumed temperature and pressure of a layer, the mass path through a homogenous layer is obtained from precalculated tables. This involves a reverse interpolation in temperature, pressure and mass path within these precalculated tables.

A linear interpolation is not, in general, sufficient. Instead, a second order reverse interpolation is performed by a Taylor series expansion around the closest point in the matrix.

$$
\begin{aligned}
V_{obs} = V_{ijk} &+ \frac{\partial V_{ijk}}{\partial T}(T - T_i) + \frac{\partial V_{ijk}}{\partial p}(p - p_j) + \frac{\partial V_{ijk}}{\partial u}(u - u_k) \\
&\left[+ \frac{\partial^2 V_{ijk}}{\partial^2 T}(T - T_i)^2 + \frac{\partial^2 V_{ijk}}{\partial^2 p}(p - p_j)^2 + \frac{\partial^2 V_{ijk}}{\partial^2 u}(u - u_k)^2 \right] \times \frac{1}{2} \\
&+ \frac{\partial^2 V_{ijk}}{\partial T \partial p}(T - T_i)(p - p_j) + \frac{\partial^2 V_{ijk}}{\partial T \partial u}(T - T_i)(u - u_k) + \frac{\partial^2 V_{ijk}}{\partial p \partial u}(p - p_j)(u - u_k)
\end{aligned}
\tag{B.1}
$$

Here V_{obs} is the observed transmission, the transmission at the nearest grid point, i, j and k the indices of the nearest grid point in temperature, pressure and mass path, respectively, T_i, p_j and u_k the temperature, pressure and mass path, respectively, used in the computation of the nearest grid point, and T, p and u the temperature, pressure and mass path corresponding to the observed transmission. All quantities are known except u and this equation forms a quadratic equation in u. Rather than determine the derivatives in this equation by finite differences involving individual transmission values in the precomputed matrix, nine parallel matrices of all of the first and second derivatives in this equation are also precalculated over the same grid. The grid spacings in temperature, pressure and mixing ratio are sufficiently fine that the interpolation from the precalculated derivatives are accurate to within the SAGE III observed uncertainty.

The nine derivatives above are found in a manner analogous to the case of fitting laboratory spectra described by Benner *et al*. [1995]. For N spectral lines the transmission at a specific wavenumber, V_λ, is the product of the transmission of each spectral line, $V_{\lambda i}$, at that wavenumber.

$$V_\lambda = \prod_{i=1}^{N} V_{\lambda i} \tag{B.2}$$

Differentiating both sides yields an expression for the derivative of the transmission with respect to a parameter, *x*, which is used in the calculation of the transmission.

$$\frac{\partial V_\lambda}{\partial x} = \sum_{i=1}^{N} \frac{V_\lambda}{V_{\lambda i}} \frac{\partial V_{\lambda i}}{\partial x} \tag{B.3}$$

This only requires that the derivative with respect to transmission be found for each spectral line individually. An equation may be derived for the second derivatives in a similar manner. The derivative for an individual spectral line is straightforward, although complicated at times. For example, SAGE III uses only Voigt spectral line shapes. The nth derivative for a Voigt spectral line with respect to the mass path, u, can be expressed in terms of only the transmission itself, the mass path and *n*.

$$\frac{\partial^n V_i}{\partial u^n} = \left(\frac{1 n V_i}{u} \right)^n V_i \tag{B.4}$$

This expression provides two of the nine required derivatives. The remaining seven derivatives involve at most only algebraic variations of the physical conditions, the spectral line parameters, the transmission and the real and imaginary parts of the complex error function. The real part of the complex error function is just the Voigt function which was used in the calculation of the transmission. Calculating both the real and imaginary parts of the complex error function requires less than twice the time required to calculate the real part.

The light falling upon a single pixel of the CCD cannot be treated as monochromatic. The transmission and derivatives must apply over a finite range of wavelength with the appropriate point spread function, $\Psi(\lambda)$, applied. This is approximated by calculations of the transmission and its derivatives at *n* specific wavelengths and it is assumed that these values are constant over a finite spectral interval, $\Delta\lambda_i$.

$$Y_{mean} = \frac{\sum_{i=1}^{n} \Psi(\lambda_i) Y_i(\lambda_i) \Delta\lambda_i}{\sum_{i=1}^{n} \Psi(\lambda_i) \Delta\lambda_i} \tag{B.5}$$

Here *Y* may represent either the transmittance or one of its derivatives.

The pressure, temperature and/or mass path as a function of position in the atmosphere are retrieved by means of a global least squares solution. The least squares process requires the derivative of the calculated transmission with respect to each unconstrained

parameter at each observed atmospheric point. These derivatives are supplied directly by interpolation in the precomputed derivative matrix. First order interpolation is done using a Taylor series expansion and the tabulated second derivatives. For example, the derivative of the transmission with respect to temperature requires four table lookups for derivatives.

$$\frac{\partial V}{\partial T} = \frac{\partial V_{ijk}}{\partial T} + \frac{\partial^2 V_{ijk}}{\partial^2 T}(T - T_i) + \frac{\partial^2 V_{ijk}}{\partial T \partial p}(p - p_j) + \frac{\partial^2 V_{ijk}}{\partial T \partial u}(u - u_k) \tag{B.6}$$

The derivative of the transmission with respect to a physical parameter in a given layer is insufficient in itself for the global least squares retrieval. The derivative of the transmission of a ray in the occultation mode with respect to a physical parameter in a specific layer requires that the derivative be propagated in the manner of Gordley and Russell [1980] through the atmosphere. For example, the derivative of the transmission V after the final layer N with respect to parameter x from layer i ($1 \le i \le N$) is accomplished with a series of derivatives of the transmission with respect to mass path in the precalculated table.

$$\frac{\partial V_N}{\partial x_i} = \frac{\partial V_i}{\partial x_i} + \prod_{j=i}^{N-1} \frac{(\partial V / \partial u)_{T_{j+1,pj+1,V_{j+1}}}}{(\partial V / \partial u)_{T_{j+1,pj+1,V_j}}} \tag{B.7}$$

For $i \ge N$, the derivative is zero.

References

Benner, D. C., C. P. Rinsland, V. Malathy Devi, M. A. H. Smith and D. Atkins, A multispectrum nonlinear least squares fitting technique, *J. Quant. Spectrosc. Radiat. Transfer*, 53, 705-721, 1995.

Gordley, L. L., and J. M. Russell, A fast and accurate radiance algorithm for applications to inversion of limb measurements, *in Remote Sensing of Atmospheres and Oceans*, edited by A. Deepak, p. 591, Academic Press, San Diego, Calif., 1980.

Appendix C. Atmospheric Inhomogeneity

The SAGE III inversion algorithm, as do essentially all processing algorithms for limb viewing instruments, assumes that the atmosphere is spherically homogeneous. This is probably a good assumption for most stratospheric constituents but is not always true for cloud and may well be a poor approximation for other constituents in the troposphere. Of all the species measured by SAGE III, cloud is most likely to be affected by its own inhomogeneous nature. Despite this, the current SAGE III algorithm, essentially an extension of that used for SAGE II [Kent *et al*., 1993], neglects this feature of cloud observations. Simulation studies are in progress that may lead to modifications in the cloud detection algorithm that exploit inhomogeneity as a tool to infer the presence of cloud. Inhomogeneous cloud, whether stratospheric or tropospheric, is likely to degrade the quality of concurrent SAGE III measurements of molecular species and temperature and pressure.

Airborne lidar data, taken on an approximately 8000 km flight path over the tropical Pacific, has been used to simulate high altitude SAGE II cloud measurements and their inversion [Kent *et al.*, 1997]. These simulations produce cloud extinction values similar in magnitude and distribution to those obtained from SAGE II. They also show the existence of three possible error conditions that result from the inhomogeneous nature of the cloud:

1. The true altitude of a cloud may be higher than that found as a result of the SAGE II inversion. Errors of 1 km or more occurred in ~40% of the data set.

2. The inverted cloud extinction may differ (biased low) from the volume averaged extinction along the horizontal ray path.

3. The presence of non-uniform or isolated cloud patches can result in an apparent negative inverted extinction value just below the cloud. Such values were observed in about one third of the simulations. The present SAGE II inversion scheme (bottom up Twomey-Chahine) suppresses these negative values but compensates by reducing the extinction value just above the offending level.

SAGE transmission measurements are an amalgamation of several independent scans across the Sun. In the presence of cloud or other inhomogeneities, these scans will measure different amounts of transmitted radiation from the same point on the Sun (because the spacecraft moves and the LOS at a given tangent altitude, as a result, also moves). These differences are manifested in the transmission data as an increased standard deviation relative to homogeneous conditions. The possibility exists that this variability may be used as a additional input to the cloud detection algorithm. The simulation described above has been extended to include spacecraft motion and compared to results from SAGE II observations.

Figure C.1 shows a scatter plot of SAGE II data at an altitude of 14.5 km in which the relative error in the slant path optical depth (SPOD) has been plotted against the SPOD itself. Low values of SPOD, corresponding to cloud-free observations, show low relative error. As cloud is observed in some scans, the relative error increases to a maximum as SPOD also increases. Then as more and more scans observe cloud, the relative error decreases as SPOD continues to increase. Figure C.2 shows the equivalent simulation using airborne lidar data. The behavior is very similar to that shown in Figure C.1. Individual data points in this figure are coded by their wavelength extinction ratio (525 to 1020 nm aerosol extinction ratio). This ratio is used as the primary discriminator between cloud and aerosol in SAGE II observations and is similar to that proposed for the SAGE III algorithm. We note that the majority of the high error cases (mixed cloud) would be identified as cloud due to their low extinction ratio. However, some high error cases have higher extinction ratios and would not be identified as cloud by the SAGE II algorithm though cloud is clearly present.

Based on these results, we plan to carry out further simulations of the effect of cloud and other inhomogeneities on the inversion algorithm and data quality (not only on cloud presence but also for all other detected species). In particular, we will investigate the effects of the Polar Stratospheric Clouds (PSCs) on data from the SAGE III/METEOR 3M flight. The outcome of further simulations may lead to modifications of the inversion algorithm (particularly for cloud detection) and error estimation. We will also consider the implication of cloud homogeneity on the SAGE III validation program (particularly its tropospheric section).

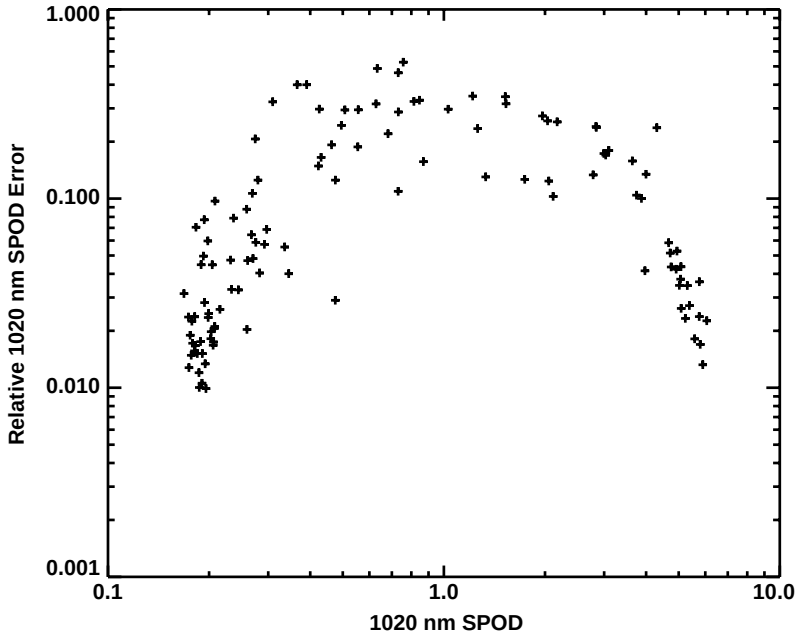

Figure C.1 A scatter plot of SAGE II data at an altitude of 14.5 km, in which the relative error in the slant path optical depth (SPOD) is plotted against the SPOD itself. Data points cover both cloudy and non-cloudy situations.

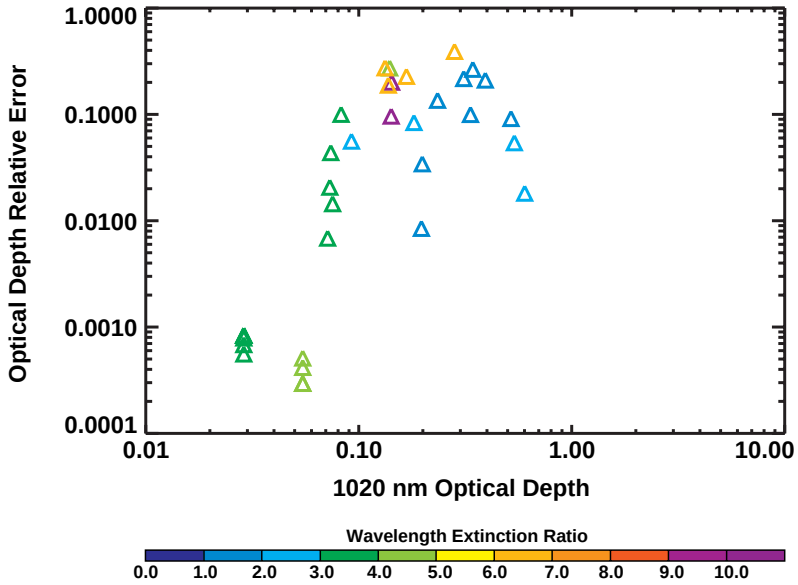

Figure C.2 Scatter plot equivalent to that shown in figure C.1, but derived from simulations based on airborne lidar data obtained within a cloud field. The color coding shows the retrieved 525 to 1020-nm aerosol extinction ratio.

References

Kent, G. S., D. M. Winker, M. T. Osborn and K. M. Skeens, A model for the separation of cloud and aerosol in SAGE II occultation data, *J. Geophys. Res.,* 98, 20725-20735, 1993.

Kent, G. S., D. M. Winker, M. A. Vaughan, P-H. Wang, and K. M. Skeens, Simulation of SAGE II cloud measurements using airborne lidar data. *J. Geophys. Res*., 102, 21,795-21,807, 1997.

Appendix D. Molecular Absorption Cross-Sections: Spectroscopic Considerations for SAGE III

D.1 Introduction

This appendix reviews the current knowledge of molecular absorption cross sections as it pertains to the SAGE III instrument, and is focused on the spectroscopic needs of the planned SAGE III measurements. This means the discussion is limited to those molecules and spectral regions that will be measured by the SAGE III instrument. Each of the individual molecules measured by SAGE III is discussed in separate sections. However, each section addresses not only that part of the spectrum which is used to measure that gas but the rest of the spectrum where absorption by that species could interfere with the retrieval of other molecules.

Since new spectroscopic measurements will be conducted over the lifetime of the SAGE III operation, improvement in the molecular absorption cross-section database will evolve with time. Therefore, the SAGE III software will utilize the most up-to-date spectroscopic data for the processing and generation of the SAGE III products.

D.2 Species Specific Information

D.2.1 Ozone

D.2.1.1 Ultraviolet

Recent Measurements

The compilation of UV ozone cross-sections for LOWTRAN 7 and MODTRAN, by G.P. Anderson *et al*. [1989] is currently recommended, at least for wavelengths up to 345 nm. This compilation is primarily based on the data of Bass and Paur [1985] from 240 to 330, including a quadratic temperature dependence. Between 180 and 240 nm the measurements of Molina and Molina [1986] are used. The measurements of Molina & Molina [1986] and Yoshino *et al*. [1988] were used to extend the temperature dependent range to 340 nm, and preliminary data of Cacciani *et al*. [1987], (later published as Cacciani *et al*. [1989]), was to extend the wavelength coverage to 365 nm.

For wavelengths from 345 to 354 nm, the room temperature values in MODTRAN are consistent with those of Molina & Molina [1986] and with those of Cacciani *et al*. [1989]. However there appears to be a problem with their temperature dependence for wavelengths greater than 345, resulting in a significant underestimate of the ozone absorption at stratospheric temperatures. The cause of this problem with the temperature dependence is not clear, (G. P. Anderson, private communication, 1996).

The recent room temperature measurements by Daumont *et al*. [1992] from 195 to 345 nm, agree within the stated accuracies with these earlier values. This group recently has extended these measurements to lower temperatures, [Malicet *et al*., 1998]. Burrows *et al*. [1999] have also measured the temperature dependence of ozone from 231 to 794 nm. These measurements, along with the recent accurate measurements of the ozone cross section for the 253.7 nm mercury line, by the University of Minnesota Group [Mauersberger, *et al*. 1986 and 1987; and Barnes and Mauersberger, 1986], should be used to re-examine the cross sections for this whole spectral region. The cross section at this mercury line based on Hearn's [1961] data was used to normalize the Bass and Paur [1985] data, along with a number of the earlier measurements.

Brion *et al*., [1998] have preliminary results continuing the room temperature measurements for ozone absorption from 345 nm to 830 nm. These should be used to extend the ozone cross sections through the gap that currently exists in the available quantitative data between 360 and 410 nm.

Estimated Accuracy

The uncertainties in the UV data are generally within 1 to 2 % for wavelengths less than 325 nm. At longer wavelengths the uncertainties become increasingly larger as the values of the absorption cross section become smaller with increasing wavelength, and the uncertainties in the zero-absorption reference value become more significant. The uncertainties are nearly 10% by 345 nm, and greater than 20% for wavelengths greater than 350 nm. In the vicinity of the absorption minimum near the SAGE 385 nm aerosol channel, the uncertainties in the absorption cross section exceeds a factor of 2. However, at this wavelength the ozone absorption is negligible compared to the aerosol attenuation and is less than 5% of the typical aerosol extinction near 30 km (and the peak ozone mixing ratio).

D.2.1.2 Visible and Near Infrared Cross-Sections:

Recent Measurements

Recently there have been several new spectroscopic studies of the ozone Chappuis and Wulf absorption bands, [Anderson *et al*., 1990, 1991,1993a, and Burkholder and Talukdar, 1994] along with measurements of the absolute cross section at selected wavelengths near the peak of the Chappuis band, [Anderson and Mauersberger, 1992], and in the near IR, [Anderson *et al*., 1993b]. Shettle and Anderson [1994] have used these to develop a new set of room temperature ozone absorption cross-sections. They normalized the spectral measurements to agree with the absolute cross-section data, within the measurement uncertainties, and smoothly joined the different sets of measurements, to provide the new cross-section over the spectral range from 407 to 1089 nm.

Burkholder and Talukdar [1994] have provided a very nice measurement of the temperature dependence of the Chappuis band [from 407 to 762 nm], where they use two identical cells to directly measure the ratio of the cross sections at 298 K and a reduced temperature between 220 and 280 K.

Estimated Accuracy

The accuracy of this data set is about 1 to 2% from about 520 nm through 800 nm, where the cross sections can be constrained by the measurements of Anderson and Mauersberger, [1992], and of Anderson *et al*., [1993b]. At the extreme wavelengths near 407 and 1089 nm, where the cross section becomes very small the uncertainties are driven by sensitivity of the measurements and possible errors in the zero absorption reference value. Near these wavelengths the uncertainties in the data can exceed 25%, decreasing to 10% near 450 nm and to less than 5% near 500 nm. At the longer wavelengths, the uncertainties in the ozone cross sections increase from 2% to 5% between 800 and 850 nm, with a further increase to about 10% near 950 nm. The recent results of Brion *et al*. [1998], tend to be systematically higher by 1% than the measurements discussed above.

Deficiency of Current Available Measurements

The most significant deficiencies in the ozone data for SAGE III are the need to extend the measurements of the temperature dependence to 180 K, to cover the full range of stratospheric temperatures and through the near IR. The latter is needed more to remove ozone as an interfering species from the SAGE measurement of aerosols and water vapor in the near IR as directly to measure ozone. While Burrows *et al*. [1999] have measured the temperature dependence in out to 794 nm, their room temperature data is systematically higher than either the Shettle and Anderson [1994] compilation or the Brion *et al*. [1998] measurements throughout the visible. These differences range from 3 to 5 % near the 600 nm Chappuis peak, to in excess of 20% near 750 nm. Also the Burrows *et al*. [1998] temperature dependence in the visible shows internal inconsistencies.

D.2.1.3 References

Anderson, G. P., F. X. Kneizys, E. P. Shettle, L. W. Abreu, J. H. Chetwynd, R. E. Huffman, and L. A. Hall, UV Spectral Simulations Using LOWTRAN 7, in *Atmospheric Propagation in the UV, Visible, IR, & MM-Wave Region and Related Systems Aspects*, AGARD Conference Proceedings No. 454, Proceedings of the AGARD Electromagnetic Wave Propagation Panel Symposium Copenhagen, Denmark, 9-13 October 1989.

Anderson, S. M., P. Hupalo, and K. Mauersberger, Rotational structure in the near-infrared absorption spectrum of ozone, *J. Chem. Phys.*, 99, 737-739, 1993a.

Anderson, S. M., P. Hupalo, and K. Mauersberger, Ozone absorption cross section measurements in the Wulf bands, *Geophys. Res. Lett.*, 20, 1579-582, 1993b.

Anderson, S. M., J. Maeder, and K. Mauersberger, Effect of isotopic substitution on the visible absorption spectrum of ozone, *J. Chem. Phys.*, 94, 6351-6357, 1991.

Anderson, S. M. and K. Mauersberger, Laser measurements of ozone absorption cross sections in the Chappuis band, *Geophys. Res. Lett.*, 19, 933-936, 1992.

Anderson, S. M., J. Morton, and K. Mauersberger, "Near-infrared absorption spectra of $^{16}O_3$ and $^{18}O_3$: Adiabatic energy of the $^1A_2$ state?, *J. Chem. Phys.*, 93, 3826-3832, 1990.

Barnes, J. and K. Mauersberger, Temperature Dependence of the Ozone Absorption Cross Section at the 253.7-nm Mercury Line, *J. Geophys. Res.*, 92, 14,861-14,864, 1987

Bass, A. M. and R. J. Paur, The ultraviolet Cross-Sections of Ozone. I. Measurements in Atmospheric Ozone, *Proceedings of the Quadrennial Ozone Symposium in Halikidi, Greece*, ed. by C. Zeferos and A. Ghaz, pp 606-616, 1985.

Brion, J. A. Chakir, J. Charbonnier, D. Daumont, C. Parisee, J. Malicet (X), Absorption Spectra Measurements for the Ozone Molecule in the 350 to 830 nm Region, *J. Atmos. Chem.*, 30, 291-299, 1985

Burkholder, J. B. and R. K. Talukdar, Temperature dependence of the ozone absorption spectrum over the wavelength range 410 to 760 nm, *Geophys. Res. Lett.*, 21, 581-584, 1994.

Burrows, J.P., A. Richter, A. Dehn, B. Deters, S. Himmelmann, S. Voigt, and J. Orphal, Atmospheric remote-sensing reference data from GOME – 2. Temperature-dependent absorption cross sections of O_3 in the 231-794 nm range, *J. Quant. Spectrosc. Radiat. Transfer*, 61, 509-517, 1999.

Cacciani, M., A. diSarra, and G. Fiocco, Laboratory Measurements of the Ozone Absorption Coefficients in the Wavelength Region 339-362 nm at Different Temperatures, Dept. of Physics, University of Roma - La Sapienza, Italy, Internal Note No. 882, 1987.

Cacciani, M., A. diSarra, and G. Fiocco, and A. Amuruso, Absolute Determination of the Cross-Sections of Ozone in the Wavelength Region 339-355nm at Temperatures 220-293K, *J. Geophys. Res.*, 94, 8485-8490, 1989.

Daumont, D., J. Brion, J. Charbonnier, and J. Malicet, Ozone UV Spectroscopy I: Absorption Cross Sections at Room Temperature, *J. Atmos. Chem.*, 15, 145-155, 1992.

Malicet, J., D. Daumont, J. Charbonnier, C. Parisse, A. Chakir, and J. Brion, Ozone UV spectroscopy. II Absorption cross-sections and temperature dependence, *J. Atmos. Chem.*, 21, 263-273, 1995.

Mauersberger, K., J. Barnes, D. Hanson, and J. Morton, Measurement of the Ozone Absorption Cross Section at the 253.7 Mercury Line, *Geophys. Res. Lett.*, 13, 671-673, 1986.

Mauersberger, K., D. Hanson, J. Barnes, and J. Morton, Ozone Vapor Pressure and Absorption Cross Section Measurements: Introduction of an Ozone Standard, *J. Geophys. Res.*, 92, 8480-8485, 1987.

Molina, L. T. and M. J. Molina, Absolute Absorption Cross Sections of Ozone in the 185-350 nm Wavelength Range, *J. Geophys. Res.*, 91, 14,501-14,509, 1986.

Shettle, E. P. and S. M. Anderson, New Visible and Near IR Ozone Cross Sections for MODTRAN, presented at the 17th Annual Review Conference on Atmospheric Transmission Models, Phillips Laboratory, Bedford, MA 7-8 June 1994.

Yoshino, K. D.E.Freeman, J.R.Esmond, and W.H.Parkinson, Absolute Absorption Cross Section Measurements of Ozone in the Wavelength Region 238-335 nm and the Temperature Dependence, *Planet. Space Sci.*, 36, 395-398, 1988.

D.2.2 Nitrogen Dioxide

Recent Measurements

SAGE II has used the NO_2 cross sections measured by Graham and Johnston [1974] and compiled by Goldman *et al*. [1978] for their retrieval of the NO_2 profiles, [Cunnold *et al*., 1991]. Since then there have been several new measurements of NO_2 absorption cross sections, [Schneider *et al*., 1987; Davidson *et al*., 1989; Amoruso *et al*., 1993; Harwood and Jones, 1994; Mérienne *et al*., 1995; and Coquart *et al*., 1995]. Unfortunately intercomparisons of these different data sets with each other and the Graham and Johnston [1974] measurements show differences as large as 1 nm in the position of the

minima and maxima of the absorption as a function of wavelength, in addition to differences of up to 10-20 % in the total cross section. One deficiency of many of these measurements (and most of the earlier ones) is they were made at resolutions of 0.5 to 2 nm which is too coarse to resolve the structure present in the absorption spectrum. Kirmse, *et al*. [1997] have concatenated several of these earlier measurements to develop a single NO_2 cross section covering 300 to 908 nm. Using the Mérienne *et al*. [1995] for the 300 to 500 nm region which includes the 420 to 460 nm region used by SAGE III for its NO_2 measurements.

Harder *et al*. [1997], provide a detailed critical evaluation of the earlier measurements, in addition to high spectral resolution (< 0.01 nm) data of their own, covering 350 to 585 nm, at temperatures between 217 and 298 K. These agree with the University of Reims data (by Courtuis) to about 4% in absolute cross section. The details of the spectral structure agree although the effects of the aliasing in the Reims data are clearly present.

Recently Yoshino *et al*. [1997] and Vandaele, *et al*. [1996 and 1998] have also made high spectral resolution (< 0.1 nm) measurements of the NO_2 cross-sections. These all show agreement with the high resolution data of Mérienne *et al*. [1995] and Harder *et al*. [1997], to 3 to 5 %. Most of these results include at least one low temperature measurement (except Yoshino *et al*., 1997). These low temperature measurements also agree to within 5%, with the spectral variations becoming more pronounced. That is the local minima decrease with decreasing temperature and the local maxima increase with decreasing temperature.

Estimated Accuracy

With an instrument such as SAGE II which uses the difference between a single minimum and maximum, the use of a pair where there are large differences between the positions and cross sections, could lead to errors as large as 50 % by using the wrong cross section data. It should be noted that the validation of the SAGE II NO_2 measurements, [Cunnold *et al*., 1991], indicate that the SAGE NO_2 data is accurate to 15%. SAGE III will retrieve the NO_2 from the structure across several minima and maxima, which should mean it is much less sensitive to the position and cross sections of individual pairs of the minima and maxima. In fact the SAGE III spectral measurements can be used to check for systematic wavelength shifts in the NO_2 absorption data used in the algorithm.

In the spectral region from 400 nm to 460 nm, where there are a number of good quality high resolution measurements available, the uncertainties in the NO_2 absorption cross sections are 3-5 %. This includes the portion of the spectrum used by SAGE III and many other instruments to determine the concentration of NO_2 in the atmosphere. From 300 nm to 400 nm and from 460 nm to 500 nm the uncertainties are 5-7 %. At longer wavelengths, which are still important to remove the contributions of NO_2 from the

measurements of other species such as aerosols or NO_3, the uncertainties are 5-10 %, and are limited to measurements with resolutions (and wavelength accuracies) of 0.5 to 2 nm, which means additional errors will be introduced in convolving them with the spectral response of the SAGE III instrument. The greatest needs for additional measurements are for high resolution data at wavelengths longer than 500 nm and for low temperature measurements at all wavelengths down to 180 K, to cover the full range of stratospheric temperatures.

D.2.2.1 References

Amoruso, A. L., G. Crescentini, G. Fiocco, and M. Volpe, New Measurements of the NO_2 Absorption Cross Section in the 440- to 460- nm region and estimates of the NO_2 - N_2O_4 Equilibrium Constant, *J. Geophys. Res.*, 98, 16,857-16,863, 1993.

Bass, A. M., A. E. Ledford Jr., and A. H. Laufer, Extinction Coefficients of NO_2 and N_2O_4, *J. Res. Natl. Bur. Stand.*, 80A, 143-166.

Coquart, B. A. Jenouvrier, and M. F. Mérienne, The NO_2 Absorption Spectrum. II: Absorption Cross-Sections at Low Temperature in the 400-500 nm Region, *J. Atmos. Chem.*, 21, 251-261. 1995.

Cunnold, D. M., J. M. Zwadony, W. P. Chu, J. P. Pommereau, F. Goutail, J. Lenoble, M. P. McCormick, R. E. Viega, D. Murcray, N. Iwagami, K. Shibasaki, P. C. Simon, and W. Peetermans, Validation of SAGE II NO_2 Measurements, *J. Geophys. Res.*, 96, 12,913-12,925, 1991.

Davidson, J. A., C. A. Cantell, A. H. McDaniel, R. E. Shetter, S. Madronich, and J. G. Calvert, Visible-Ultraviolet Absorption Cross Sections for NO_2 as a Function of Temperature, *J. Geophys. Res.*, 93, 7105-7112, 1989.

Frost, G. J., L. M. Goss, and V. Vaida, Measurements of High-Resolution Ultraviolet-Visible absorption Cross Sections at Stratospheric Temperatures: 1. Nitrogen Dioxide, *J. Geophys. Res.*, 101, 3869-3877, 1996.

Graham, R. and H.S.Johnston, Photochemistry of NO_x and HNO_x Compounds, *Can. J. Chem.*, 52, 1415-1423, 1974. [Values tabulated by A.Goldman, U. of Denver]

Hall, T. C. and F. E. Blacet, Separation of the Absorption Spectra of NO_2 and N_2O_4 in the range 2400-5000 D, *J. Chem. Phys.*, 20, 1745-1749, 1952.

Harder, J. W. J. W.Brault, P. V. Johnston, and G. H. Mount, Temperature Dependent NO_2 Cross Sections at High Spectral Resolution, *J. Geophys. Res.*, 102, 3861-3879. 1997.

Harwood, M. H. and R. L. Jones, Temperature Dependent Ultraviolet-Visible Absorption Cross-Sections of NO_2 and N_2O_4: Low-Temperature Measurements of the Equilibrium Constant for $2NO_2$ W N_2O_4, *J. Geophys. Res.*, 99, 22,955-22,964, 1994.

Mérienne, M. F., A. Jenouvier, B. Coquart, The NO_2 Absorption Spectrum. I: Absorption Cross-Sections at Ambient Temperature in the 300-500 nm Region, *J. Atmos. Chem.*, 20, 281-297. 1995.

Schneider, W. G., G. K. Moortgat, G. S. Tyndall, and J. P. Burrows, Absorption Cross Sections of NO_2 in the UV and Visible Region (200-700 nm) at 298 K, *J. Photochem. Photobiol. A Chem.*, 40, 195-217, 1987.

Vandaele, A. C., C. Hermans, P. C. Simon, M. Carleer, R. Colin, S. Fally, M. F. Merienne, A. Jenouvrier, and B. Coquart, Measurements of the NO_2 absorption cross-sections from 42,000 cm^{-1} to 10,000 cm^{-1} (238-1000 nm) at 220 K and 294 K, *J. Quant. Spectrosc. Radiat. Transfer*, 59, 171-184, 1998.

Yoshino, K., J. R. Esmond, W. H. Parkinson, High-resolution absorption cross section measurements of NO_2 in the UV and visible region, *Chem. Phys.*, 221, 169-174. 1997.

D.2.3 Oxygen

Accurate knowledge of the oxygen absorption cross sections is critical for the SAGE III Experiment, since the SAGE III oxygen measurements are used to establish the atmospheric density, temperature, and pressure profiles. In addition to the direct scientific need for these profiles, they are also needed to remove the molecular Rayleigh scattering contribution from the measurements of other species at all wavelengths, and for the retrieval of the mixing ratio of the other gaseous species on pressure surfaces. This removes the need for an external source of this data, such as the NMC analyses which were used for the SAGE I and II instruments. To retrieve the oxygen density, from which the atmospheric density, temperature, and pressure profiles will be derived, SAGE III will use differential absorption measurements across the oxygen A-band from 755 to 775 nm.

The Ritter and Wilkerson [1986] measurements of the oxygen A-band with a stated accuracy of about 2%, appear to be the best of the available data. They have been adapted by Chance [1995] for use with the Global Ozone Monitoring Experiment (GOME).

However, their band strength is higher than the all of the previous measurements that they include in their Table IV, exceeding the next highest by nearly 5%, the mean by 11%, and exceeding by 15% the data of Miller *et al*. [1969], (with a stated accuracy of 4%), which are the basis of the 1992 HITRAN database, [Rothman *et al*., 1992]. Ritter and Wilkerson's [1986] line widths are near the middle of the range of the previous measurements, which have a 30% range of values. However, while the 1996 HITRAN database adapted the Ritter and Wilkerson [1986] line strengths, it continues to utilize the line widths of Givers *et al*. [1974], which are at the low end of the available measurements.

Recently Brown and Plymate [1999] have measured the oxygen A-band. The line positions, line intensities and pressure-broadening coefficients of 44 transitions in the oxygen A-band near 760 nm (from 13040 to 13168 cm^{-1}) have been calibrated using laboratory data recorded at 0.02 cm^{-1} resolution with the Fourier transform spectrometer at Kitt Peak in Arizona. The pressure-broadening coefficients for self-broadened and nitrogen-broadened widths and pressure-induced shifts in line positions have been measured through J" = 24; these have been combined and modeled with a polynomial expressed as a function of the upper state quantum number in order to compute the corresponding air-broadened line shape coefficients associated with Voigt profiles. The temperature dependence of the line widths has been determined from absorption spectra obtained with gas samples temperatures between 205 K and 297 K

The measured intensities demonstrate that the values selected for the 1996 HITRAN database are valid to within 1%. However, the line positions are in error by 0.002 to 0.015 cm^{-1} and the widths by 7 to 20%. Although the individual new measurements of temperature dependence of widths have uncertainties of 15%, the average of new measured values is within 2% of the mean value previously selected by HITRAN.

D.2.3.1 References

Brown, L. R. and C. Plymate, Experimental line parameters of the oxygen A-band at 760 nm., *submitted to J. Mol. Spectrosc,* 1999.

Brown, L. R. and R. A. Toth, Laboratory Spectroscopy of SAGE Molecules, Unpublished Manuscript, 1995.

Chance, K., O_2 A-band Studies for Cloud Detection and Algorithm Improvement, Contact Report for ESA, 1995.

Giver, L. P., R. W. Boese, and J. H. Miller, Intensity Measurements, Self-Broadening Coefficients, and Rotational Intensity Distribution for Lines of the Oxygen B Band at 6880 C, *J. Quant. Spectrosc. Radiat. Transfer*, 14, 793-802, 1974.

Miller, J. H., R. W. Boese, and L. P. Giver, Intensity Measurements and Rotational Intensity Distribution for the Oxygen A-band, *J. Quant. Spectrosc. Radiat. Transfer*, 9, 1507-1517, 1969.

Newnham, D. A., and J. Ballard, Visible absorption cross sections and integrated absorption intensities of molecular oxygen (O_2 and O_4), *J. Geophys. Res.*, 103, 28,801-28,816, 1998.

Ritter, K. J. and T. D. Wilkerson, High Resolution Spectroscopy of the Oxygen A-band, *J. Molec. Spectrosc.*, 121, 1-19, 1987.

Rothman, L. S., R. R. Gamache, R. H. Tipping, C. P. Rinsland, M. A. H. Smith, D. C. Benner, V. M. Devi, J.-M. Flaud, C. Camy-Peyret, A. Perrin, A. Goldman, S. T. Massie, L. R. Brown, and R. A. Toth, The HITRAN Molecular Database Editions of 1991 and 1992, *J. Quant. Spectrosc. Radiat. Transfer*, 48, 469-507, 1992.

Rothman, L. S. C. P. Rinsland, A. Goldman, S. T. Massie, D. P. Edwards, J.-M. Flaud, A. Perrin, C. Camy-Peyret, V. Dana, J.-Y. Mandin, J. Schroeder, A. McCann, R. R. Gamache, R. B. Watson, K. Yoshino, K. V. Chance, K. W. Jucks, L. R. Brown, V. Nemtchinov, and P. Varanasi, The HITRAN molecular spectroscopic database and HAWKS (HITRAN Atmospheric WorKStation): 1996 edition, *J. Quant. Spectrosc. Radiat. Transfer*, 60, 665-710, 1998.

D.2.4 Water Vapor

To measure atmospheric water vapor SAGE III will use differential absorption in the near IR water band from 920 to 960 nm. The HITRAN database, Rothman [1992], based on the measurements of Chevillard *et al*. [1989], provides the best available spectroscopic data, in this region. This is an improvement over the 1982 edition of the HITRAN database used by Chu *et al*. [1993] for the water vapor retrievals from SAGE II. However as noted by Brown and Toth [1995], this band is a complex of 10 interacting vibrational states and a complete theoretical modeling has not been accomplished to date, limiting the ability to give a complete accurate listing of the line positions, intensities, and spectral assignments. Recently Giver *et al*. [1999] have reported that there were systematic errors in implementing the line intensities of water vapor into the HITRAN database, which affects all the visible and near IR water bands with wavelengths less than 1200 nm. For the band centered around 940 nm, which will be used by SAGE III to retrieve water vapor, this correction amounts to a 14.4 % increase in all the lines derived from the data of Chevillard *et al*. [1989], which applies to most of the lines in this band. There are a number of weak lines in this region due to $H_2{}^{17}O$ and $H_2{}^{18}O$, and a few

unassigned lines. It is presently not clear whether this correction applies to any of these lines; however, altogether they contribute only about 1% of the total band strength.

The reported accuracies of the Chevillard *et al*. [1989] data are 7 to 50 %, depending on the spectral line. Given the 50 % uncertainties apply to the weakest lines, when integrated over the 2 nm resolution of the SAGE III detector, the water vapor absorption is known to about 10 to 15 %. To achieve greater accuracy for water vapor retrievals will require new measurements of the water vapor spectroscopy in the near IR.

Recently Brown *et al*. [1999, unpublished manuscript], have obtained new measurements of the water vapor lines for the 940 nm band. The line positions and line intensities of some 2600 transitions have been retrieved from 17 absorption spectra recorded at 0.01 and 0.02 cm^{-1} resolution using the Fourier transform spectrometer at Kitt Peak in Arizona. These have been combined with published analyses for isotopic water (H_2-^{16}O-^{18}O and H_2-^{16}O-^{17}O) to produce a new line list of some 4130 transitions from 9676.8789 to 11386.2119 cm^{-1}. Available air-broadened and self-broadened line widths from other vibrational bands at 6 μm and 2.1 μm have been inserted for A- and B- type transitions of bands in the 0.96 μm region. There are no new data for pressure-shifts and temperature dependences, however.

This study will correct the conversion mistakes recently uncovered in the visible line parameters of water by completely replacing the current 0.96 μm list in HITRAN and GEISA with better quality measurements (0.001 cm^{-1} for positions and 3% for the intensities). The individual intensities range from 6.5 E^{-22} to 1.0 E^{-27} cm^{-1}/(molecule cm^{-2}) at 296 K.

D.2.4.1 References

Brown, L. R. and R. A. Toth, Laboratory Spectroscopy of SAGE Molecules, Unpublished Manuscript, 1995.

Chevillard, J.-P., J.-Y. Mandin, J.-M. Flaud, and C. Camy-Peyret, $H_2{}^{16}O$: Line positions and intensities between 9500 and 11500 cm^{-1}. The interacting vibrational states (041), (220), (121), (022), 9300), (201), (102), and (003), *Can. J. Phys.*, 67, 1065-1084,1989.

Chu, W. P., E. W. Chiou, J. C. Larsen, L. W. Thomason, D. Rind, J. J. Buglia, S. Oltsman, M. P. McCormick, and L. M. McMaster, Algorithms and sensitivity analyses for Stratospheric Aerosol and Gas Experiment II water vapor retrieval, *J. Geophys. Res.*, 98, 4857-4866, 1993.

Giver, L. P., C. Chackerian, and P. Varanasi, Visible and Near-Infrared $H_2{}^{16}O$ Line Intensity Corrections for HITRAN-96, *to be published in J. Quantat. Spectrosc. Radiative Transf.*, 1999.

Rothman, L. S., R. R. Gamache, R. H. Tipping, C. P. Rinsland, M. A. H.Smith, D. C. Benner, V. M. Devi, J.-M. Flaud, C. Camy-Peyret, A. Perrin, A. Goldman, S. T. Massie, L. R. Brown, and R. A. Toth,, The HITRAN Molecular Database Editions of 1991 and 1992, *J. Quant. Spectrosc. Radiat. Transfer*, 48, 469-507, 1992.

Rothman, L. S., R. R.Gamache, A. Barbe, A. Goldman, J. R. Gillis, L. R. Brown, R. A. Toth, J.-M. Flaud, and C. Camy-Peyret, AFGL atmospheric absorption line parameters compilation: 1982 edition, *Appl. Opt.*, 22, 2247-2256, 1983.

Rothman, L. S. C. P. Rinsland, A. Goldman, S. T. Massie, D. P. Edwards, J.-M. Flaud, A. Perrin, C. Camy-Peyret, V. Dana, J.-Y. Mandin, J. Schroeder, A. McCann, R. R. Gamache, R. B. Watson, K. Yoshino, K. V. Chance, K. W. Jucks, L. R. Brown, V. Nemtchinov, and P. Varanasi, The HITRAN molecular spectroscopic database and HAWKS (HITRAN Atmospheric WorKStation): 1996 edition, *J. Quant. Spectrosc. Radiat. Transfer*, 60, 665-710, 1998.

D.2.5 The Nitrate Free Radical NO_3

SAGE III utilizing differential absorption spectroscopy in the 640 to 680 nm region will measure the nitrate free radical NO_3. It is at least a weak absorber throughout the visible, although strong absorption features and 623 and 662 nm dominate its visible spectrum. A general review of the Nitrate Free Radical NO_3, including its spectroscopy, is given by Wayne *et al*. [1991].

DeMore *et al*. [1997] recommend using an average of the studies by Marinelli *et al*. [1982], Ravishankara and Wine [1983], Burrows *et al*. [1985], Ravishankara and Mauldin [1986], Sander [1986], Canosa-Mas *et al*. [1987], and Cantrell *et al*. [1987] for the cross section at the 662 nm peak at room temperature. There is disagreement in the temperature dependence with Cantrell *et al*. [1987] finding the absorption to be independent of temperature between 215 and 348 K, and Ravishankara and Mauldin [1986] and Sander [1986] reporting the cross section increasing with decreasing temperature. For the cross section increase, Ravishankara and Mauldin report 40 % between 298 and 220 K and Sanders 20 % between 298 and 230 K. The recent measurements of Yokelson *et al*. [1994] tend to support the temperature dependence of Sanders. Yokelson *et al*. also note that their measurements can be considered to supersede the earlier results of Ravishankara and Mauldin [1987].

The uncertainties in the absorption cross sections are 10-15 % at room temperature and 20-25 % at stratospheric temperatures. Given this result in a corresponding uncertainty of the retrieved NO_3 amounts, improved measurements are needed.

D.2.5.1 References

Burrows, J. P., G. S. Tyndall, and G. K. Moortgat, Absorption spectrum of NO_3 and kinetics of the reactions of NO_3 with NO_2, Cl, and several stable atmospheric species at 298 K, *J. Chem. Phys.*, 89, 4848-4856, 1985.

Canosa-Mas, C. E., M. Fowles, P. J. Houghton, and R. P. Wayne, Absolute absorption cross section measurements on NO_3, *J. Chem. Soc. Faraday Trans. II*, 83, 1465-1474, 1987.

Cantrell, C. A., J. A. Davidson, R. E. Shetter, B. A. Anderson, and J. G. Calvert, The temperature Invariance of the NO_3 absorption cross section in the 662 nm region, *J. Phys. Chem.*, 91, 5858-5863, 1987.

DeMore, W. B., S. P. Sander, D. M. Golden, R. F. Hampson, M. J. Kurylo, C. J. Howard, A. R. Ravishankara, C. E. Kolb, and M. J. Molina, *Chemical Kinetics and Photochemical Data for Use in Stratospheric Modeling Evaluation Number 11*, JPL Publication 94-26, 1994.

DeMore, W. B., S. P. Sander, D. M. Golden, R. F. Hampson, M. J. Kurylo, C. J. Howard, A. R. Ravishankara, C. E. Kolb, M. J. Molina, *Chemical Kinetics and Photochemical Data for Use in Stratospheric Modeling Evaluation Number 12*, JPL Publication 97-4, 1997.

Marinelli, W. J., D. M. Swanson, and H. S. Johnston, Absorption cross sections and line shape for the NO_3 (0-0) band, *J. Chem. Phys.*, 76, 2864-2870, 1982.

Ravishankara, A. R. and R. L. Mauldin III, Temperature dependence of NO_3 cross section in the 662-nm region, *J. Geophys. Res.*, 91, 8709-8712, 1986.

Ravishankara, A. R. and P. H. Wine, Absorption Cross Sections for NO_3 between 565 and 673 nm, *Chem. Phys. Lettr.*, 101, 73-78, 1983.

Sanders, S.P. (1986) Temperature dependence of the NO_3 absorption spectrum, *J. Chem. Phys.*, 90, 4135-4142.

Wayne, R. P., I. Barnes, P. Biggs, J. P. Burrows, C. E. Canosa-Mas, J. Hjorth, G. Le Bras, G. K. Moortgat, D. Perner, G. Poulet, G. Restlli, and H. Sidebottom, The

Nitrate Radical: Physics, Chemistry, and the Atmosphere, *Atmos. Envirn.*, 25A, 1-203, 1991.

Yokelson, R. J., J. B. Burkholder, R. W. Fox, R. K. Talukdar, and A. R. Ravishankara, Temperature Dependence of the NO_3 Absorption Spectrum, *J. Phys. Chem.*, 98, 13,144-150, 1994.

D.2.6 Symmetric Chlorine Dioxide OClO

Symmetric chlorine dioxide, OClO, has a series of absorption peaks between 280 and 480 nm , which reach a maximum near 351 nm. The region from 380 to 420 nm will be used for the SAGE III retrievals of OClO. While there have been a number of spectroscopic studies of OClO, relatively few experiments have provided absolute cross sections at room temperature, with apparently only Wahner *et al*. [1987] examining the temperature dependence. Frost *et al*. (1996) have recently reported a spectroscopic study of OClO at stratospheric temperatures (200 ± 20 K); however, using two different techniques to convert this data to absolute cross sections, report differences of 50%. DeMore *et al*. [1994] recommend the Wahner *et al*. [1987] absorption cross sections. These data have a reported accuracy of 3-5 %.

D.2.6.1 References

DeMore, W. B., S. P. Sander, D. M. Golden, R. F.Hampson, M. J. Kurylo, C. J. Howard, A. R. Ravishankara, C. E. Kolb, M. J. Molina, *Chemical Kinetics and Photochemical Data for Use in Stratospheric Modeling Evaluation Number 11*, JPL Publication 94-26, 1994.

Frost, G. J., L. M. Goss, and V. Vaida, Measurements of High-Resolution Ultraviolet-Visible absorption Cross Sections at Stratospheric Temperatures: 2. Chlorine dioxide, *J. Geophys. Res.*, 101, 3879-3884, 1996.

Wahner, A., G. S. Tyndall, and A. R. Ravishankara, Absorption cross sections for OClO as a function of temperature in the wavelength range 240-480 nm, *J. Phys. Chem.*, 91, 2734-2738, 1987.

Appendix E. Lunar Altitude Registration

The tangent height registration for the lunar radiometric measurements can be accomplished using a technique similar to the solar method described in the SAGE III Algorithm Theoretical Basis Document, Transmission Level 1B Products, Section 3.2.3. To accomplish the tangent height registration, the primary requirement is to accurately determine the position on the lunar limb, in angular units, of the measurement position. Meeting this requirement is complicated by the scanning motion of the instrument field of view over the target (moon), resulting in the radiometric measurements being taken at irregular points on the target limb, and the absence of accurate absolute pointing information from the instrument. Additionally, the instrument is designed to focus the scan plane through the radiometric center of the moon, which, unlike the case of the sun as the target, does not coincide with the geometric center of the moon. Information provided by the instrument used in the calculations to meet the limb position registration requirement includes the time of the radiometric measurement and the accurate relative pointing information derived from the movement of the instrument scan mirror. At each time increment, a detailed ephemeris calculation can be accomplished that solves the geometry data parameters for the spacecraft to Earth and moon. These ephemeris calculations provide the geometry position information from the spacecraft to the moon center, top, and bottom limbs.

To perform the tangent height registration, additional information will be required from a radiance model of the moon. Information required from the model includes the radiance center, terminator location, and rotation to the scan plane of the instrument. A radiance model is currently being developed as part of the NASA Earth Observing Spacecraft Mission by the U.S. Geological Survey and Northern Arizona University as Project ROLO. The radiance map of the moon, required as an input to the SAGE III model, could be the Project ROLO data when it becomes available, or some alternative to-be-determined source.

The tangent height computations are accomplished using the following steps:

1. A radiometric model predicts the radiometric center of the moon and establishes whether the upper or lower limb of the moon is inside the lunar terminator line.

2. The scan azimuth angle in angular units relative to the target is determined by the difference between the ephemeris calculated velocity to target angle and the measured relative azimuth change of the instrument.

3. An edge signature is established and used to accurately locate the first observation that falls on the top or bottom edge of the lunar disk. The edge signature is established using the second derivative inflection point as the edge crossing time.

4. A geometric height correction is calculated for the first observation based on the offset of the radiometric center of the moon from the geometric center of the moon, and the scan azimuth angle. The geometric height correction, in angular units, is applied to the first observation to correct for the height difference between the (known) height of the top (or bottom) of the lunar disk and the offset height of the first observation.

5. Relative scan mirror elevation movement is used to calculate the angular positions of the subsequent observation points on the lunar limb.

6. The refracted tangent altitude of each observation point is then computed from the angular positions using the same processing routine as the solar processing procedure.